JOURNAL OF GEOPHYSICAL RESEARCH, VOL. 104, NO. C6, PAGES 13,359–13,379, JUNE 15, 1999

Mesoscale eddies, satellite altimetry, and new production in the Sargasso Sea

David A. Siegel[1]

Institute for Computational Earth System Science, University of California, Santa Barbara

Dennis J. McGillicuddy Jr.

Department of Applied Ocean Physics and Engineering, Woods Hole Oceanographic Institution
Woods Hole, Massachusetts

Erik A. Fields

Institute for Computational Earth System Science, University of California, Santa Barbara

Abstract. Satellite altimetry and hydrographic observations are used to characterize the mesoscale eddy field in the Sargasso Sea near Bermuda and to address the role of physical processes on the supply of new nutrients to the euphotic zone. The observed sea level anomaly (SLA) field is dominated by the occurrence of westward propagating features with SLA signatures as large as 25 cm, Eulerian temporal scales of roughly a month, lifetimes of several months, spatial scales of ~200 km, and a propagation of ~5 cm s^{-1}. Hydrographic estimates of dynamic height anomaly (referenced to 4000 dbar) are well correlated with satellite SLA ($r^2 = 0.65$), and at least 85% of the observed dynamic height variability is associated with the first baroclinic mode of motion. This allows us to apply the satellite observations to remotely estimate isopycnal displacements and the flux of nutrients into the euphotic zone due to eddy pumping. Eddy pumping is the process by which mesoscale eddies induce isopycnal displacements that lift nutrient-replete waters into the euphotic zone, driving new primary production. A kinematic approach to the estimation of the eddy pumping results in a flux of 0.24 ± 0.1 mol N m^{-2} yr^{-1} (including a scale estimate for the small contribution due to 18° water eddies). This flux is more than an order of magnitude larger than the diapycnal diffusive flux as well as scale estimates for the vertical transport due to isopycnal mixing along sloping isopycnal surfaces. Eddy pumping and wintertime convection are the two dominant mechanisms transporting new nutrients into the euphotic zone, and the sum of all physical new nutrient supply fluxes effectively balances previous geochemical estimates of annual new production for this site. However, if biological transports (e.g., nitrogen fixation, etc.) are significant, the new nitrogen supply budget will be in excess of geochemical new production estimates. This suggests that the various physical and biological transport fluxes, as well as geochemical inferences of new production, still need to be reconciled and many outstanding questions remain.

1. Introduction

Understanding new production, the rate at which new nutrients are incorporated into the marine ecosystem, is critical for the assessment of the ocean's role in the fate of anthropogenic carbon dioxide emissions [e.g., *Eppley and Peterson*, 1979; *Sarmiento and Le Quéré*, 1996]. Assuming that the marine ecosystem is at steady state on annual timescales, the input of new nutrients to the euphotic zone must be balanced by the export of organic materials to the aphotic zone. This removal of euphotic zone carbon concentrations by export, either on sinking particles or by physical advective and diffusive processes, occurs on the seasonal to interannual timescales which are critical for understanding the interactions of the ocean's biological pump with anthropogenic CO_2 concentrations [e.g., *Sarmiento et al.*, 1995; *Ducklow et al.*, 1995].

Rates of new primary production can be determined directly by the measurement of the uptake of labeled nitrate, the primary new nitrogen source, by phytoplankton [*Dugdale and Goering*, 1967]. Unfortunately, in oligotrophic waters, such as are found in the Sargasso Sea, direct determination of ^{15}N-labeled nitrate incorporation is complicated by the extremely low ambient nutrient concentrations (F. Lipschultz, personal communication, 1996). Hence new production rates are often determined by inference, assuming that inputs of new nutrients are balanced by the export of organic materials [e.g., *Eppley and Peterson*, 1979; *Jenkins and Wallace*, 1992]. These methods include the collection of sinking particles using sediment traps, determination of the disequilibrium of naturally occurring

---

[1] Also at Donald Bren School of Environmental Science and Management and Department of Geography, University of California, Santa Barbara.

Copyright 1999 by the American Geophysical Union.

Paper number 1999JC900051.
0148-0227/99/1999JC900051$09.00

Table 1. New Production Estimates for the Sargasso Sea

	Annual Flux, mol N m^{-2} yr^{-1}	Reference
Sediment trap fluxes	0.19	*Altabet* [1989]
	0.10	*Lohrenz et al.* [1992]
	0.11 ± 0.07	BATS PON flux 150 m*
Thorium export (ThE)	0.14	*Buesseler* [1998]†
O_2 utilization	0.48 ± 0.10	*Jenkins and Wallace* [1992]
	0.42 ± 0.09	*Jenkins and Goldman* [1985]
	0.91 ± 0.10	*Sarmiento et al.* [1990]
	0.42 ± 0.23	*Sarmiento et al.* [1990]‡
O_2 production	0.46 ± 0.09	*Jenkins and Goldman* [1985]
	0.39 ± 0.16	*Spitzer and Jenkins* [1989]
	0.51 ± 0.14	*Spitzer and Jenkins* [1989]
^{3}He flux gauge	0.56 ± 0.16	*Jenkins* [1988]
	0.47 ± 0.15	W. Jenkins (personal communication, 1997)§
	0.7 ± 0.2	*Jenkins* [1998]
Mean new production	0.50 ± 0.15	

*Mean flux and standard deviation estimates were determined over the period December 1988 to January 1997 from the Bermuda Atlantic Time-series Study (BATS) database (http://www.bbsr.edu/bats/). PON is particulate organic nitrogen.

†Summertime export only is included. Values were converted to nitrogen units using a constant Redfield ratio.

‡The O_2 utilization rate was corrected for lateral transport of nitrate using the results of *Rintoul and Wunsch* [1991].

§An expansion of the *Jenkins* [1988] estimate was performed to include the entire late 1980s data set collected at station S.

radioactive tracer fields (i.e., ^{238}U:^{234}Th), the production rate of dissolved oxygen concentrations in the euphotic zone, the consumption rate of oxygen in the aphotic zone, as well as the modeling of dissolved gas inventories. A select summary of new nitrogen flux estimates for the Sargasso Sea is presented in Table 1. It is apparent that rates determined from the collection of sinking fluxes of particulate materials are considerably lower than those determined from dissolved gas inventories. This discrepancy may be due in part to the various sampling issues experienced by surface-tethered sediment trap arrays [e.g., *Michaels et al*., 1990, 1994a; *Buesseler*, 1992; *Gust et al*., 1992; *Buesseler et al*., 1994]. Excluding trap-derived estimates, new production rates are roughly 0.5 mol N m^{-2} yr^{-1}. These geochemically based rates of new production are much larger than can be explained by a simple one-dimensional balance where vertical turbulent diffusion supplies the new nitrate utilized in the euphotic zone [e.g., *Jenkins*, 1988; *Musgrave et al*., 1988]. A main purpose of this contribution is to quantify the roles that physical mechanisms play in the supply of new nitrogen to the euphotic zone.

Mesoscale physical phenomena have long been thought to influence upper ocean biogeochemistry through the horizontal advection of biogeochemically relevant materials and/or their influence on net vertical transport [e.g., *Woods*, 1988; *Falkowski et al*., 1991; *Flierl and Davis*, 1993; *Strass*, 1992; *Dickey et al*., 1993; *Robinson et al*., 1993; *McGillicuddy et al*., 1995, 1998; *Siegel and Deuser*, 1997; *McGillicuddy and Robinson*, 1997; *Oschlies and Garçon*, 1998]. Eddies influence biogeochemical stocks and rates by horizontal advection and lateral stirring of water masses, the tilting of isopycnal surfaces enabling vertical transport by isopycnal mixing, and the uplift of nutrient-rich, isopycnal surfaces into the euphotic zone. The characteristic time and space scales for open ocean mesoscale motions are of order of a week to several months and over many tens to a couple hundred kilometers. These space and timescales effectively match typical open ocean ecosystem scales, suggesting that eddies may have an important role in regulating biogeochemical cycles in the open ocean ecosystems [e.g., *Haury et al*., 1978].

The recent process modeling of *McGillicuddy and Robinson* [1997] (hereinafter referred to as MR97) examined a mechanism by which mesoscale eddies create a net upward transport of new nutrients into the euphotic zone (Figure 1). Formation and intensification of cyclonic eddies lift nutrient-replete isopycnals into the euphotic zone, where those nutrients are rapidly utilized by phytoplankton. In the downwelling case, anticyclonic features simply push nutrient-depleted waters out of the euphotic zone. Hence eddy-induced vertical transport of new nutrients is rectified by the asymmetry imposed by the vertical gradient of the in situ light field. The timescale for remineralization of nutrients (~10 days) is generally shorter than a typical eddy lifetime (many months); hence nutrient concentrations within the aphotic zone will be restored to their equilibrium concentrations by remineralization. MR97 have argued that eddy pumping provides the "missing" summertime transport of new nutrients into the euphotic zone of the Sargasso Sea.

Mesoscale features may be detected using sea level observations provided by satellite altimeters. In a cyclonic eddy the water column will be denser than normal, which results in a lower than average sea level height or a negative sea level anomaly (SLA). In these features, isopycnal surfaces will be uplifted toward the euphotic zone and incorporation of nutrient-rich waters can occur. Anticyclonic features (high SLA) will depress isopycnals out of the euphotic zone, transporting nutrient-depleted water downward. The highly successful TOPEX/POSEIDON (T/P) satellite altimetry mission has provided sea level observations that cover nearly the entire globe with a repeat schedule of ~10 days and an accuracy for SLA of better than 3 cm [e.g., *Fu et al*., 1994; *LeTraon and Ogor*, 1998]. Over the subtropical oceans, adjacent T/P altimeter track lines are ~250 km apart, which is considerably larger than the internal Rossby radius of deformation (~40 km). Hence it is difficult to use T/P data alone to diagnose mesoscale processes. Coverage of ocean mesoscale processes can be improved by combining observations from the T/P mission with data from other satellite altimeters such as the European Remote Sensing Satellite (ERS) [e.g., *LeTraon et al*., 1995]. The widespread availability of long-term, accurate altimetric data (T/P began operations in late 1992) provides an excellent opportunity to assess the role of eddies in open ocean biogeochemistry.

We present an analysis of sea level variability in the vicinity of the U.S. Joint Global Flux Study (JGOFS) Bermuda Atlantic Time-series Study (BATS) using satellite altimetry and hydrographic data sets. The primary objectives are to characterize the mesoscale eddy field about the BATS site and to quantify the physical processes that supply new nutrients to the euphotic zone. The next section describes the processing and sampling methods for the altimetric and hydrographic data sets. Results using the altimetric data set are presented, followed by an analysis of the BATS hydrographic record. The discussion focuses on quantification of the relevant physical processes that transport new nitrogen into the euphotic zone and an attempt to close the new nitrogen supply budget at BATS. The paper ends by assessing the implications of the

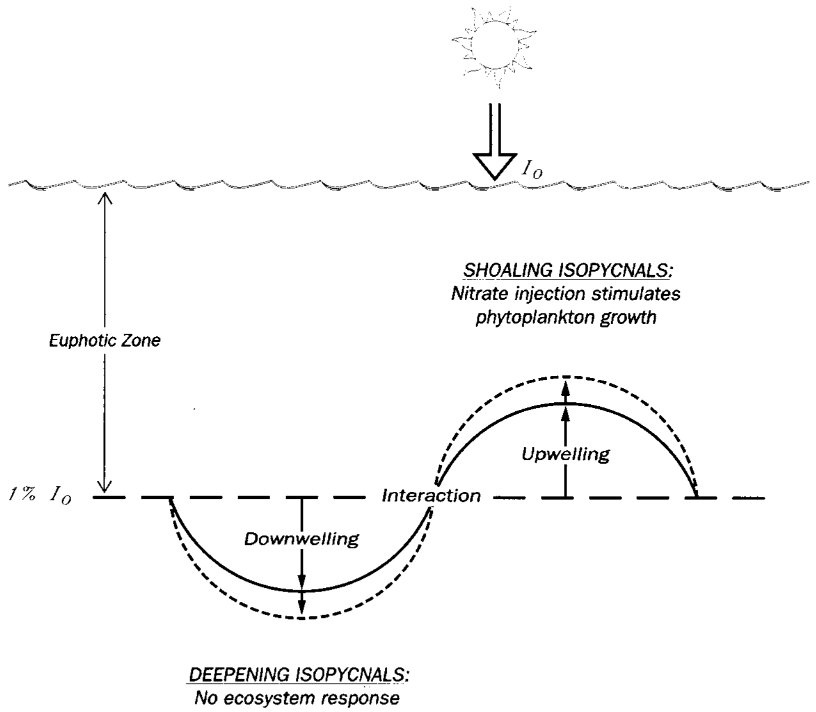

Figure 1. Cartoon representation of the eddy upwelling mechanism. The formation and intensification of cyclonic (anticyclonic) eddy will result in a low (high) sea level anomaly (SLA) signal and an upwelling (downwelling) of isopycnal surfaces. A net transport of new nutrients occurs as upwelling lifts nutrient-replete waters into the euphotic zone, where they are utilized by phytoplankton; whereas a downwelling will push nutrient-depleted waters into the aphotic zone, where will be no ecosystem response. Reprinted by permission from *Nature* [*McGillicuddy et al.*, 1998], copyright (1998) Macmillan Magazines Ltd.

assumptions used and their importance toward the development of a predictive understanding of new production.

2. Data

2.1. Satellite Altimetry

Merged geophysical TOPEX/POSEIDON data records were processed following *Bernada* [1993] except that the Center for Space Research CSR3.0 ocean tide model was used [*Eanes and Bettadpur*, 1995]. The resulting residual sea surface height (RSSH) data where smoothed along track and assigned to reference passes following the procedures outlined by *Polito and Cornillon* [1997]. A 3-year mean (T/P cycles 2–114) is removed from the RSSH estimates to produce estimates of sea level anomaly. The removal of the long-term mean removes the mean circulation and geoid signals. Slightly over 4 years of T/P altimetry, October 1992 to December 1996, were used in this study. The T/P altimeter samples along an exact repeat orbit of ~10 days. The resulting spacing between track lines is 265 and 560 km in the zonal and meridional directions respectively, at 32°N.

To increase coverage of mesoscale processes, satellite altimetry data from European Remote Sensing Satellites 1 and 2 (ERS 1 and 2) were used. Merged SLA data were provided by *Archiving, Validation, and Interpretation of Satellite Data in Oceanography* (*AVISO*) [1997]. The ERS and T/P data sets are merged through a global minimization of dual crossover differences [*LeTraon et al.*, 1995; *LeTraon and Ogor*, 1998]. This provided ERS orbits with accuracy similar to T/P, ~2 cm rms [*AVISO*, 1997]. The ERS exact repeat cycle is 35 days, which results in a typical cross-track spacing of 65 and 285 km for the zonal and meridional directions, respectively. Unfortunately, no exact repeat cycle data are available for 1994, as ERS 1 conducted a gravity mapping mission.

Fields of SLA were determined using an objective analysis (OA) mapping routine modified from *Carter and Robinson* [1987]. This procedure was used to produce spatial distributions of SLA and its associated uncertainty. Objectively analyzed fields are made on a ~45-km regular grid resolution for a 900-km by 900-km domain centered on the BATS site (32°N 64°W, Plate 1). The correlation model used was calculated using T/P along-track data as well as hydrographic data from the U.S. JGOFS BATS project (see appendix for details). In addition, SLA estimates were also objectively analyzed at the location of the BATS site in order to compare with the hydrographic data set.

An example of an OA-determined field of SLA, with the associated uncertainty field, for November 3, 1993, is shown in Plate 1. Results from using T/P data alone are shown in the Plate 1, top, while the merged T/P and ERS 1 results are shown in Plate 1, bottom. Plate 1, left, gives the interpolated SLA fields, and Plate 1, right, shows the percent of mapping error variance relative to the measurement error. The locations of observations form a "chain-link fence" pattern. This depiction shows similar patterns with or without the ERS data (Plate 1). However, the expected error levels within the "T/P diamonds" are much lower using the merged data set. Without ERS data, error levels are often greater than 50% for much of the domain. Including the ERS altimetry, error values drop considerably and are never greater than 50%. It should be noted that

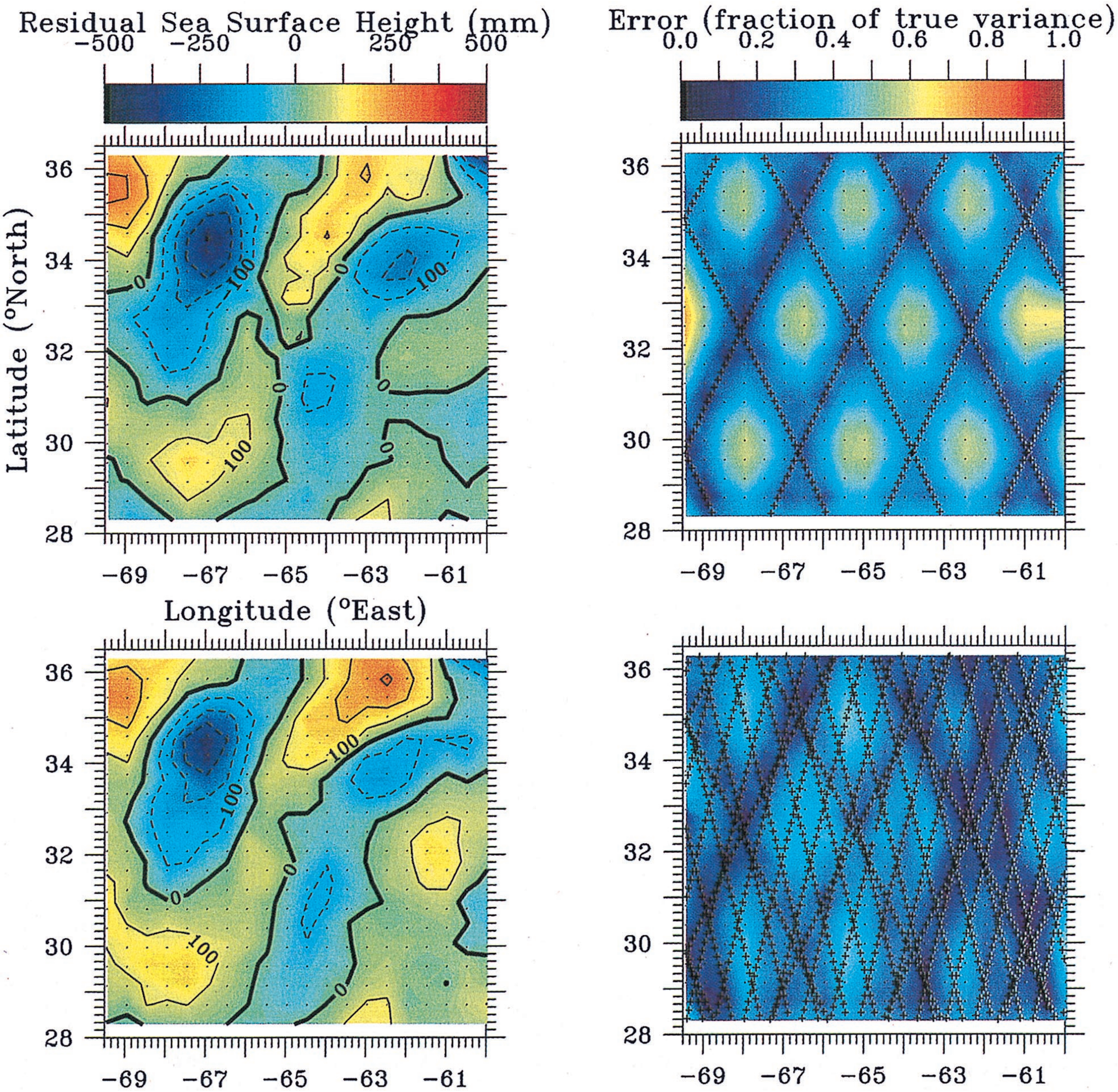

Plate 1. An example of objective analysis (OA) determined fields of (left) SLA and (right) SLA associated uncertainty fields for November 3, 1993, (top) without and (bottom) with the ERS 1 data. Levels of uncertainty are quantified in terms of the percent of the objective mapping error variance relative to the measurement error variance.

the patterns in the expected error distributions and the differences between the two error maps will be robust, whereas absolute levels are sensitive to the exact nature of the correlation function computations.

2.2. BATS Hydrography

The BATS station (31°50′N, 64°10′W) is located ~75 km southeast of the island of Bermuda in the Sargasso Sea [*Michaels and Knap*, 1996]. The bottom depth at the BATS site is ~4680 m. The BATS site is occupied 16 times each year, and a nearly complete suite of hydrographic and biogeochemical variables are sampled. Sampling started in October 1988, and we use these data until December 1996 (data displayed may be less, depending upon their availability). The sampling frequency is typically monthly, although biweekly sampling is conducted during the spring bloom period (January through April). For present purposes, full water column conductivity-temperature-depth (CTD) profiles are used to estimate isopycnal displacements and dynamic height anomalies for comparison with the altimetric OA estimates at the BATS site. All calculations of dynamic height anomaly, $\Delta D(0/4000\ \mathrm{dbar})$, use a reference isobar of 4000 dbar. Nitrate concentrations (actually $NO_3 + NO_2$) were also determined from discrete water samples during these or other nearby casts. All sampling and analysis protocols used in the U.S. JGOFS BATS program are well documented [*Michaels et al.*, 1994b; *Michaels and Knap*, 1996]. The spatial distribution of the climatological mean dynamic height anomaly and its associated geostrophic circulation are calculated from the National Oceanic and Atmospheric Administration 1994 (NOAA94) ocean climatology

[*Levitus and Boyer*, 1994; *Levitus et al.*, 1994] using a reference isobar of 4000 dbar.

3. Satellite Altimeter Analyses

A time sequence of five objectively mapped SLA fields and corresponding current vectors shows plan view structures of many, fairly large, closed circulation features with a sense of westward propagation (Plate 2). The time between successive SLA fields is 2 weeks, and the period spans August 25 to October 20, 1993, and current vectors are calculated assuming that the geostrophic relationship holds [$u_E = (-g/f)\partial \mathrm{SLA}/\partial y$ and $v_E = (g/f)\partial \mathrm{SLA}/\partial x$, where g is the gravitational acceleration and f is the local Coriolis parameter]. In general, the eddy features propagate westward, their spatial extents are ~200 km, and their SLA amplitudes are 20 to 30 cm. There is no sense of a propagation of these features in the meridional direction. For the time period shown in Plate 2, SLA changes at the exact location of the BATS site are very small ($\leq$10 cm) while large-amplitude SLA features ($\geq$25 cm) are seen throughout the region. There are also a good deal of merging and interactions between adjacent features (Plate 2). An animated version of the SLA fields and eddy currents for the entire record (October 1992 to December 1996) is available via the world wide web (http://www.icess.ucsb.edu/~davey/TP_BATS/BATS_sla_currents.mpg).

Spatial distributions of the root-mean-square (rms) SLA and eddy kinetic energy [EKE $= 1/2(u^2 + v^2)^{1/2}$] show the expected low levels of eddy energy in the Sargasso Sea with significantly elevated levels to the north (Plates 3a and 3b). Values of rms SLA and EKE are consistent with climatologies produced by analyses of dynamic height, moored current meter, SOFAR float, and drifter data sets [*Owens et al.*, 1982; *Richardson*, 1983, 1993; *Siegel and Deuser*, 1997]. There appears to be little zonal variation in EKE while a slight zonal increase in rms SLA is observed in the western portion of the domain. Near BATS, values of rms SLA and EKE are ~9.0 cm and 115 $\mathrm{cm^2\ s^{-2}}$, respectively.

The mean geostrophic current patterns derived from the NOAA94 Ocean Atlas show a very weak westward flow near BATS ($U = -0.5\ \mathrm{cm\ s^{-1}}$, $V = 0.1\ \mathrm{cm\ s^{-1}}$) and a stronger east-northeastward flow (as much as 11 $\mathrm{cm\ s^{-1}}$) to the north-northwest of the BATS site (Plate 3c). In this depiction the domain mean dynamic height is subtracted to give dynamic height anomaly in units of dynamic millimeters. Weak westward flow is observed as is expected within the Gulf Stream recirculation zone [*Worthington*, 1976]. Mean kinetic energy (MKE) levels are much smaller near BATS, with values of 0.13 $\mathrm{m^2\ s^{-2}}$, resulting in a ratio of EKE to MKE of ~900, again consistent with long-term observations from the Sargasso Sea [e.g., *Owens et al.*, 1982; *Siegel and Deuser*, 1997]. The large-scale gradients in the north show a highly smoothed representation of the southern edge of the Gulf Stream and are due to the large degree of spatial and temporal filtering used in constructing the NOAA94 Ocean Atlas [*Levitus and Boyer*, 1994; *Levitus et al.*, 1994].

The time-longitude and time-latitude SLA distributions at the latitude and longitude of BATS (31.66°N and 64.50°W) from October 1992 to December 1996 are dominated by the occurrence of westward propagating features with SLA signatures often greater than 30 cm with little consistent propagation in the meridional direction (Plates 4a and 4b). Westward propagation speeds are ~5 $\mathrm{cm\ s^{-1}}$, in agreement with previous findings [e.g., *The MODE Group*, 1978; *Richman et al.*, 1977]. In general, Eulerian timescales are roughly a month or two and spatial scales are ~200 km. The time-longitude SLA distribution (Plate 4a) also shows indications of annual period oscillations in SLA. These oscillations are not in phase with the seasonal heating cycle for the Sargasso Sea, where increases in steric height would be expected in the summer. These signals are probably related to the annual period, wind-forced Rossby wave motions discussed by *Polito and Cornillon* [1997]. However, a detailed analysis of these factors is beyond the scope of this contribution. Superimposed on this annual SLA signal are many shorter-period, energetic features that propagate westward (Plate 4a). The time-latitude distributions (Plate 4b) show the expected result of higher SLA variability toward the north and no obvious sense of meridional propagation or annual variability.

4. Hydrographic Data Analyses

Determinations of dynamic height anomalies from the BATS CTD observations, $\Delta D(0/4000\ \mathrm{dbar})$, are well correlated with altimeter SLA estimates objectively mapped to the BATS site (Figure 2). Typical SLA amplitudes are of order 20 cm with temporal timescales of variability of ~30 days, and no apparent seasonal variations are observed. Approximately 65% of the variance in $\Delta D(0/4000\ \mathrm{dbar})$ is explained by the altimetric time series. This indicates that the satellite determinations of sea level are reflecting primarily the baroclinic modes of motion. It should also be noted that at BATS, only once is an SLA feature observed with a magnitude less than -12 cm (Figure 2). This contrasts with the -25-cm SLA features often seen in the vicinity of this site (Plates 2 and 4).

Mean vertical profiles of potential density σ_θ show the seasonal pycnocline capping the weakly stratified, 18° water mass, which in turn overlies the main pycnocline (Figure 3a). The potential density of the 18° water is roughly 26.4, and its boundaries may be assessed using the mean density gradient profile [e.g., *Talley and Raymer*, 1982]. Low values of the mean density gradient delineate the 18° water mass between 200 and 500 m (typical buoyancy frequency values are ~1.5 cph), which is surrounded by higher buoyancy frequencies within the seasonal pycnocline (roughly 6.5 cph) and the main pycnocline (~2.7 cph).

Mean nitrate concentrations are below detectability within the euphotic zone, and values increase rapidly with depth (Figure 3b). This pattern reflects the basic processes of light-induced consumption within the euphotic zone and the remineralization of organic nitrogen to inorganic forms below this zone. The mean depth of the nitracline, the depth above which nitrate concentrations are not detectable using standard autoanalyzer techniques, is ~80 m. Below this depth, nitrate concentrations increase with depth until a deep maximum is observed near 1000 m (not shown). Values of nitrate concentration increase slowly within the 18° water mass (from ~3 to 5 $\mu\mathrm{mol\ kg^{-1}}$, Figure 3b).

Below the surface layer the hydrographic data can be used to determine the displacement of isopycnal surfaces assuming a local balance between time rate of change of density and its vertical advection or

$$\eta_\sigma(z, t) = \frac{\sigma_\theta(z, t) - \langle\sigma_\theta(z)\rangle}{\partial\langle\sigma_\theta(z)\rangle/\partial z} \qquad (1)$$

where $\sigma_\theta(z, t)$ is the measured value of potential density, $\langle\sigma_\theta(z)\rangle$ is its mean value, $\partial\langle\sigma_\theta(z)\rangle/\partial z$ is the gradient of

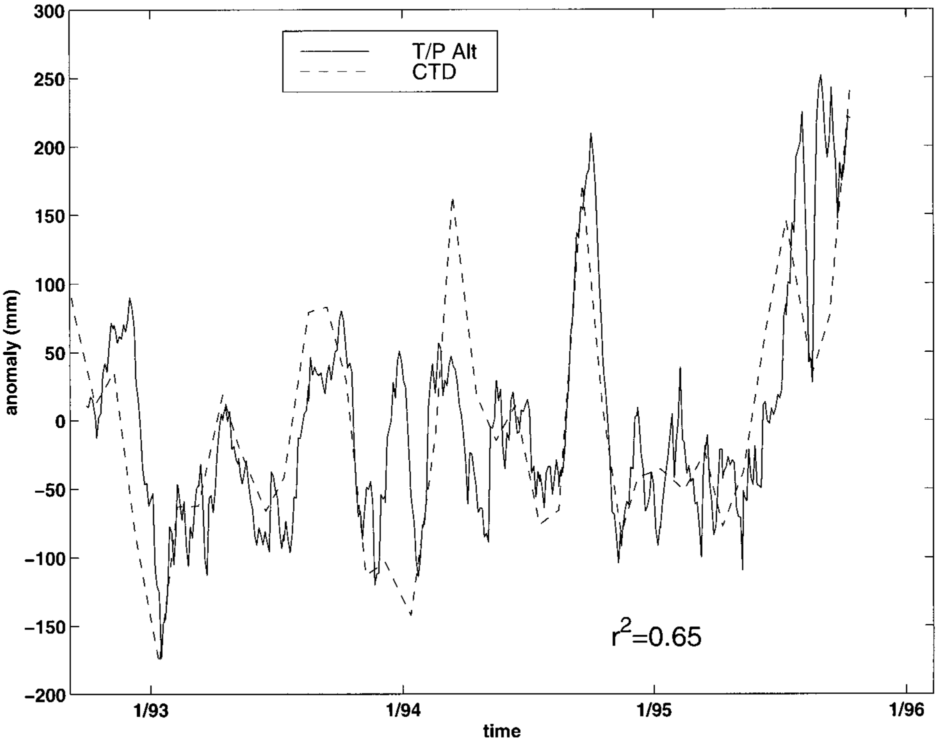

Figure 2. Time series of SLA objectively analyzed to the BATS site (solid line) and dynamic height anomaly, $\Delta D(0/4000$ dbar), from the available BATS hydrographic record (dashed line). The squared correlation coefficient between the two time series is 0.65. Estimates of SLA are objectively analyzed to the BATS site with a time interval of 3 days.

$\langle\sigma_\theta(z)\rangle$, and t is time. A similar displacement can be defined for isonutrient surfaces. The time history of isopycnal, $\eta_\sigma(z, t)$, and isonutrient displacements, $\eta_N(z, t)$, for depths of 200, 400, 600, and 800 m are shown in Figure 4. Hydrographic data are shown for the available BATS data set (October 1988 to December 1995). Also shown is the time series of $\Delta D(0/4000$ dbar) (and SLA estimates when available) scaled to match the displacement estimates (see below). Isopycnal and isonutrient surfaces are deflected by as much as 100 m from their mean locations. Root-mean-square values for both isopycnal and

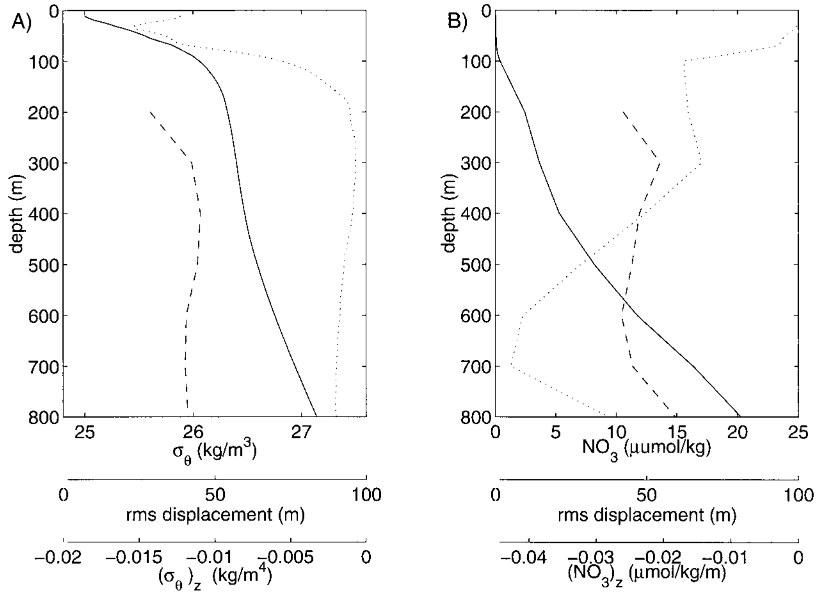

Figure 3. Mean (solid line), mean gradient (dotted line), and rms vertical displacement (dashed line) profiles for (a) potential density and (b) nitrate concentration from the entire BATS hydrographic sampling (October 1988 to December 1996). Vertical displacement profiles are not shown for depths above 200 m.

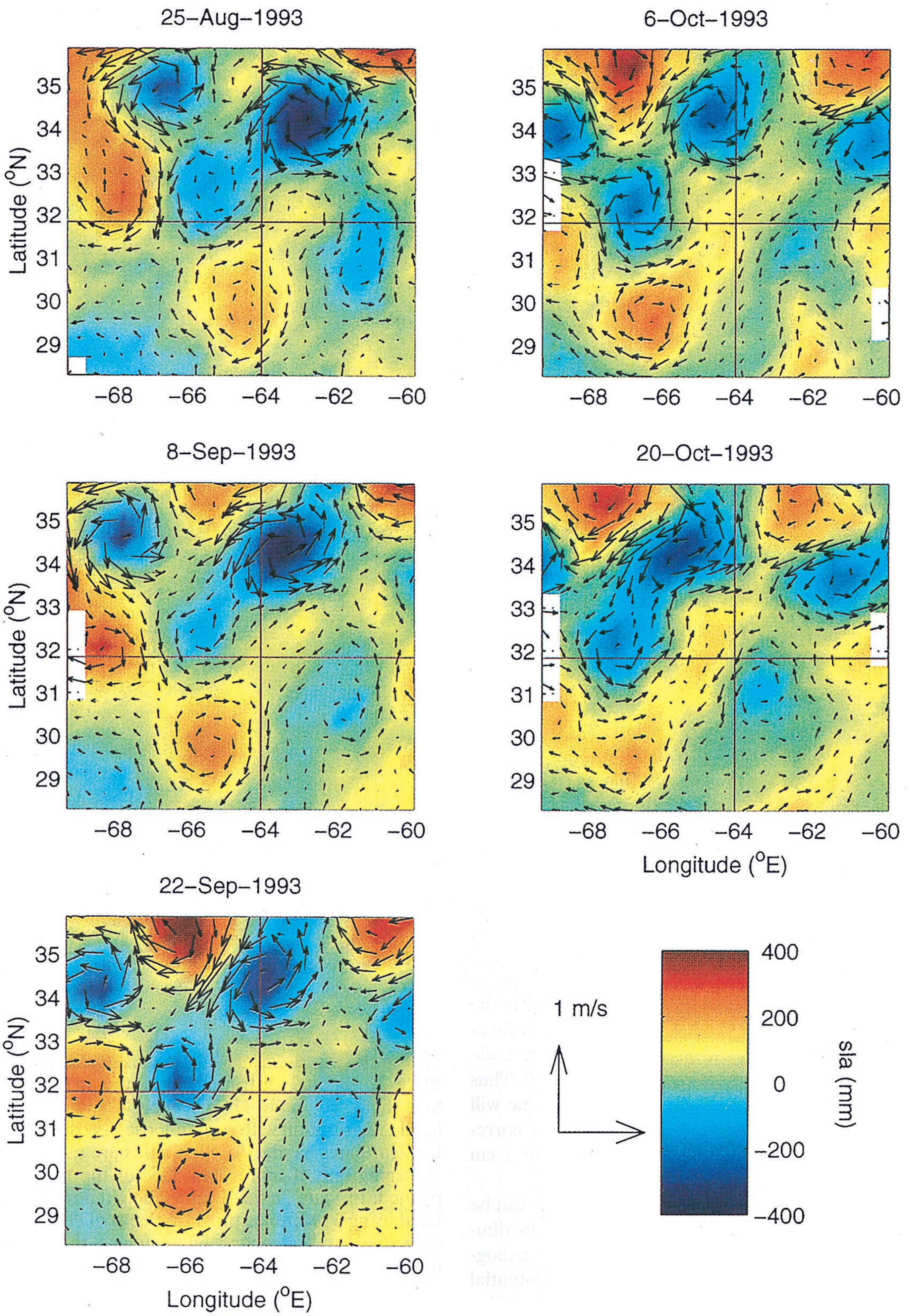

Plate 2. Five biweekly TOPEX/POSEIDON (T/P) and ERS 1 merged analyses of SLA and geostrophic eddy currents for analysis dates of August 25, September 8, September 22, October 6, and October 20 (all 1993). The SLA fields are colored with red, representing high sea level, and blue, indicating low sea level. The SLA color bar (in mm) and the length of the eddy current vectors are indicated at bottom right. The Bermuda Atlantic Time-series Study (BATS) site is at the crosshairs near the center of the analyzed domain. The eddy current vectors are calculated from the mapped SLA fields assuming that the geostrophic relationship holds [$u_E = (-g/f)\partial \mathrm{SLA}/\partial y$ and $v_E = (g/f)\partial \mathrm{SLA}/\partial x$]. Estimates of the small mean geostrophic velocity field (Plate 3c) are not included in this depiction.

isonutrient displacements are typically ~50 m, and these rms estimates are roughly constant from 200 to 1000 m (Figures 3a and 3b). In addition, estimates of isopycnal displacements have a high degree of vertical coherence for depths greater than 200 m as well as with the dynamic height anomaly (Figure 4).

Changes in the depth of isopycnal $[\eta_\sigma(z, t)]$ and isonutrient $[\eta_N(z, t)]$ surfaces are often well correlated with each other $(r^2 > 0.8)$ within the upper portion of the main thermocline (Figure 4). This indicates that on synoptic timescales the dominant process regulating changes in potential density and nutrient concentrations is the same (e.g., vertical advection). The correlation degrades in the upper ocean, indicating that different processes are regulating changes in the observed potential density and nutrient concentration. The correlation between $\eta_\sigma(z, t)$ and $\eta_N(z, t)$ surfaces also degrades as the deep nitrate maximum is approached ($|z| \geq \sim 800$ m, Figure 4).

A correspondence between measures of dynamic topography and the displacement of various isopycnal surfaces is also observed where isopycnal surfaces are depressed when $\Delta D(0/4000$ dbar) is elevated (Figure 4). The vertical profile of the squared regression coefficient r^2 between estimates of $\Delta D(0/4000$ dbar) and $\eta_\sigma(z, t)$ and between $\Delta D(0/4000$ dbar) and $\eta_N(z, t)$ as well as regression slopes for these relationships (meter displacement per centimeter dynamic topography) are shown in Figure 5. Below a depth of ~300 m this empirical relationship is highly significant, explaining more than 50% of the variance. Typical slopes are -4 m of isosurface displacement per centimeter of dynamic topography, independent of whether it is calculated using potential density or nitrate concentration (Figure 5). Hence an SLA feature with an amplitude of 25 cm will represent a 100-m displacement of isopycnal surfaces throughout much of the main thermocline.

The relationship between isopycnal depth and sea level can be diagnosed through analysis of a two-layer, free surface, baroclinic ocean [e.g., *Gill*, 1982]. For this system the perturbation depth of the upper layer η is related to the sea level anomaly by

$$\frac{\eta}{\mathrm{SLA}} \approx -\frac{\rho_o H}{\Delta\rho H_2} \qquad (2)$$

where $\Delta\rho$ is the density difference between the two layers (~2 kg m^{-3}), ρ_o is a scaling density (1026 kg m^{-3}), H is the ocean depth (4700 m), and H_2 is the depth of the lower layer when the ocean is at rest (≈4200 m). Applying these scale estimates to (2) results in a value for η/SLA of ~ -560. Thus a 5.6-m upward vertical displacement of the thermocline will result from a 1-cm SLA depression. This derived value corresponds well with the -4-m isopycnal displacement per 1 cm SLA observed in Figure 5.

The vertical structure of the isopycnal displacements can be further evaluated by determining the vertical mode distribution from the hydrographic time series. An empirical orthogonal function (EOF) analysis of the 7-year BATS potential density data is dominated by the first three EOF modes, which explain more than 95% of the total variance (Figure 6). In determining the EOF modes, the upper 200 m of the water column is ignored to eliminate the influence of seasonal variations on the potential density field [*Gavart and DeMey*, 1997]. The first mode explains 88.5% of the variance of the density structure and has a vertical structure nearly identical to the first dynamical baroclinic mode for density (Figure 6; see below). The vertical structure of the first EOF mode depicts the main thermocline "heaving" up and down over the upper 1500 m. The amplitude function time series for the first EOF mode explains 76% of the variance in $\Delta D(0/4000$ dbar). This indicates that the dominant fraction of the SLA variability is associated with the first baroclinic mode. The second EOF mode explains nearly 5% of the total variance in potential density with a vertical mode structure, suggesting an "accordion" structure throughout a depth range from 200 to 1200 m. These EOF analysis results differ from calculations made by

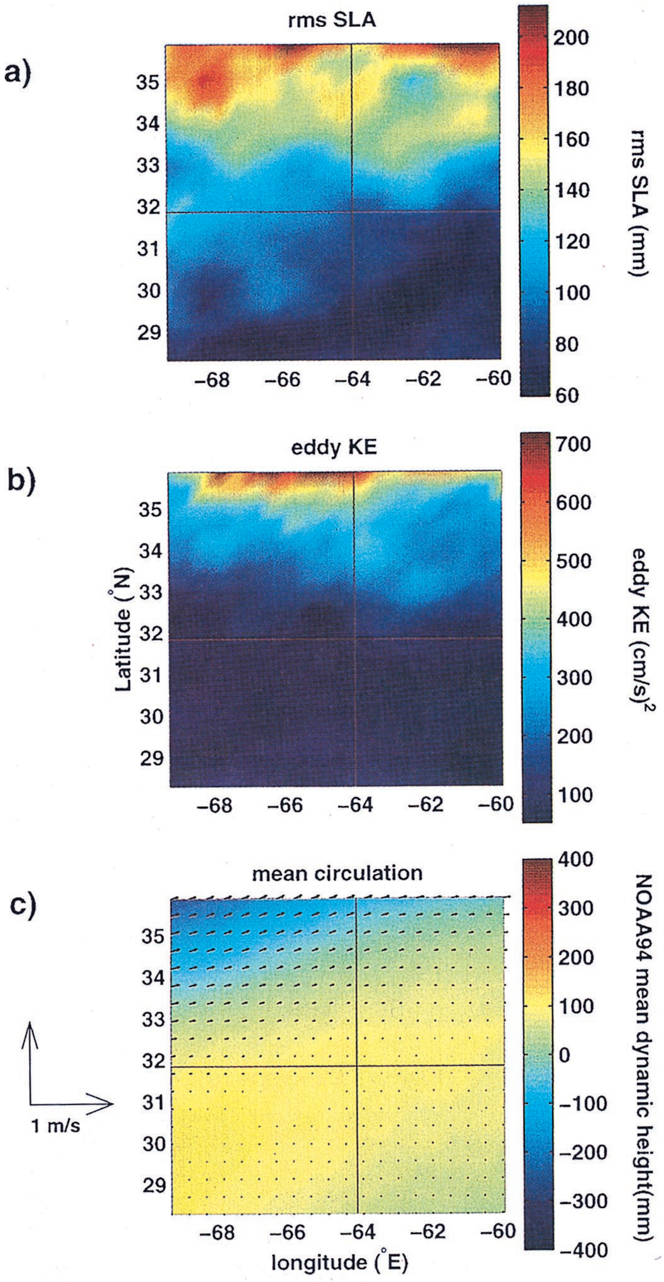

Plate 3. Spatial distributions of the (a) root-mean-square SLA field, (b) eddy kinetic energy, and (c) mean dynamic height distribution with superimposed geostrophic current vectors. In Plates 3a and 3b, SLA fields are used in the ensemble averaging only if more than 50% of the true variance is explained. In Plate 3c the dynamic height anomaly field is calculated using a reference pressure depth of 4000 dbar and anomaly values are calculated by removing the domain-averaged mean.

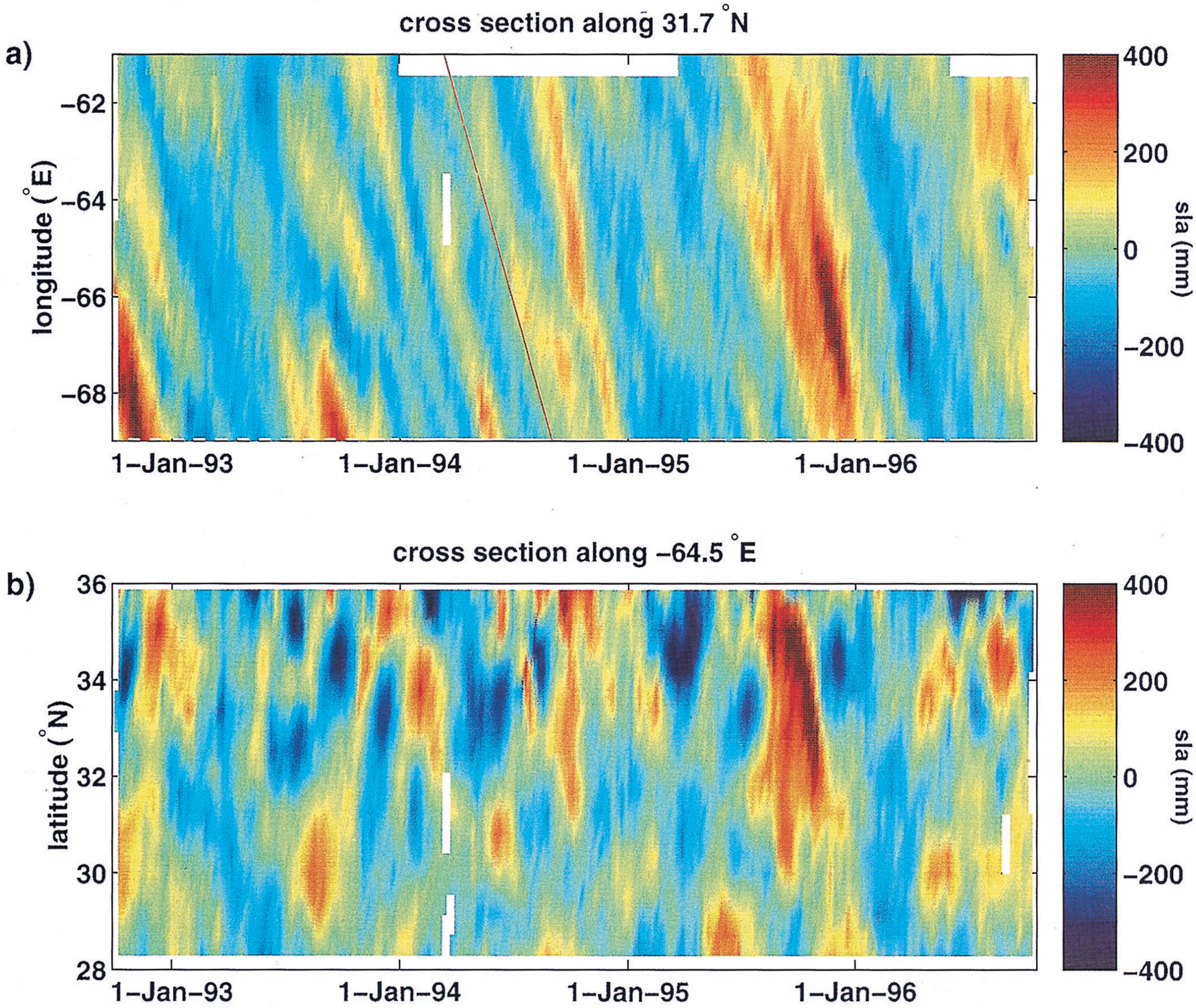

Plate 4. Time-distance plots of SLA along the (a) latitude and (b) longitude of the BATS site (31.66°N, 64.50°W). Estimates of SLA are shown only if their OA uncertainty levels are less than 50%. The inclined red line in Plate 4a represents a zonal propagation speed of 5 cm s^{-1}.

Frankignoul [1981] using the nearby station S data set, probably owing to the wide vertical spacing between levels and the relatively small fraction of the entire water column used in his calculations.

Dynamical modes of variability can be calculated from the mean buoyancy frequency profile [$N^2 = -(g/\rho_o)\partial\langle\rho\rangle/\partial z$] by solving the vertical structure function for the stream function [e.g., *Gill*, 1982; *McWilliams et al.*, 1986; *Lippert and Briscoe*, 1990] or

$$\frac{d}{dz}\left[\frac{1}{N^2(z)}\frac{d\hat{\Psi}}{dz}\right] + \gamma\hat{\Psi} = 0 \qquad (3)$$

where $\hat{\Psi}$ is the structure function for the stream function. This assumes that the ocean is linear, flat bottomed, and without a mean flow. This eigensystem is solved, using the shooting method, for a series of eigenmodes $\hat{\Psi}_n$, for each eigenvalue γ_n, assuming rigid upper and lower boundary conditions ($d\hat{\Psi}/dz = 0$ on these boundaries). By assuming geostrophy and a hydrostatic balance, the dynamical modes for the stream function can be used to determine modes for density perturbation $\hat{\rho}_n$ or

$$\hat{\rho}_n = -\frac{\rho_o f_o}{g}\frac{\partial \hat{\Psi}_n}{\partial z} \qquad (4)$$

The first three baroclinic modes for potential density calculated using the BATS hydrographic data are shown in Figure 6. The zeroth mode is the barotropic mode and is not relevant to addressing vertical density fluctuations and displacements. The vertical structure of the first dynamical mode looks almost exactly the same as the first EOF mode, while the shapes of the second modes show only moderate similarity (Figure 6).

The eigenvalue γ_n from the solution of (3) can be used to determine the internal Rossby radius of deformation [$R_n = 1/(f_o^2\gamma_n)^{1/2}$, where f_o is the local Coriolis parameter] and the maximum phase speed ($c_n = -\beta R_n^2$, where $\beta = df/dy$) for each mode [*Gill*, 1982]. The maximum phase speeds for the first three baroclinic modes are 2.8, 0.44, and 0.23 cm s^{-1}, respectively. The first-mode theoretical phase speed is about

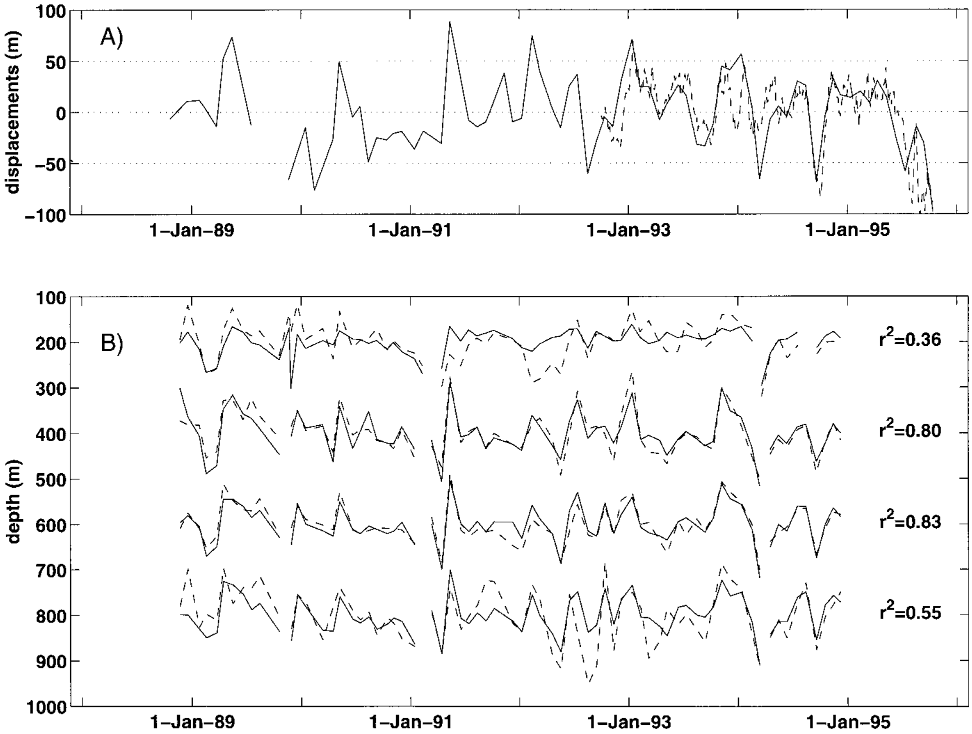

Figure 4. (a) Time series of $\Delta D(0/4000$ dbar) (solid line) and altimetric SLA (dashed line, when available) scaled to represent isosurface displacements at 200 m (see text). (b) Isopycnal (solid line) and isonutrient (dashed line) displacement time series for depths of 200, 400, 600, and 800 m for the entire BATS time series. Also shown in Figure 4b are the correlation coefficients (r^2) between the isopycnal and isonutrient surfaces.

one half of the observed zonal SLA propagation speed (~5 cm s^{-1}, Plate 4a). This result is consistent with the observations made by *Chelton and Schlax* [1996].

The dynamical modes can also be used as a basis set to determine the partitioning of density variance into different vertical modes [e.g., *Wunsch*, 1997]. This amounts to modeling the vertical density fluctuation profile, $\tilde{\rho}(z, t)$, as a linear combination of dynamical modes or

$$\tilde{\rho}(z, t) = \sum_{n=0}^{N_{\max}} \alpha_{\rho n}(t)\hat{\rho}_n(z) + n_\rho(z, t) \tag{5}$$

where $N_{\max}$ is the maximum number of modes used in the model fit ($N_{\max} = 5$), $\alpha_{\rho n}(t)$ is the time-dependent weighting function for the density modes, and $n_\rho(z, t)$ is the residual noise that is minimized in estimating $\alpha_{\rho n}(t)$. The results of this calculation illustrate that the first two modes contain more than 95% of the variance and that the first dynamical mode alone explains 85% of the variance. The first dynamic mode's amplitude function, $\alpha_{\rho 1}(t)$, is correlated with $\Delta D(0/4000$ dbar) ($r^2 = 0.76$). These basic results do not change when the number of modes used in the fit, $N_{\max}$, is varied from 2 to 8. This, as well as the other evidence presented, demonstrates that the dominant portion of the vertical density variability in the main thermocline is associated with the first baroclinic mode of motion.

5. Discussion

We have shown that the spatial and temporal structure of mesoscale features in the vicinity of the BATS site are consistent with previous investigations of the mesoscale dynamics in the Sargasso Sea [e.g., *Richman et al.*, 1977; *The MODE Group*, 1978; *McWilliams et al.*, 1983]. In the following we will estimate annual rates of physical transport of new nutrients into the euphotic zone and will compare these estimates with geochemical determinations of new production. Last, we will discuss the importance of understanding how open ocean, mesoscale eddies transport and retain water parcels.

5.1. Vertical Nutrient Transport by Eddy Pumping

Here we introduce a kinematic approach for estimating the eddy-pumping flux. We assume that uplifted nutrients are utilized instantaneously within the euphotic zone while nutrient concentrations are restored to their equilibrium values below this region. By determining the maximum uplift during the passage of an individual eddy and knowing the relationship between isopycnal displacement and nutrient concentration, a displaced nutrient profile can be determined. For each upwelling event the eddy-pumping flux is simply the displaced nutrient content in the euphotic zone. This approach is similar to the nutrient model incorporated by *McGillicuddy and Robinson* [1997] and assumes that the timescale between uplifting events is much longer than the remineralization timescale within the aphotic zone. Consistent with this assumption, low SLA features are observed every 60 days or so (Plate 4 and Figure 2), which is much longer than typically assumed remineralization timescales (~10 days) [*Doney et al.*, 1996; MR97]. Hence the present calculation should be a faithful representation of the essential processes regulating the eddy-pumping flux.

The details of the kinematic eddy-pumping calculation are

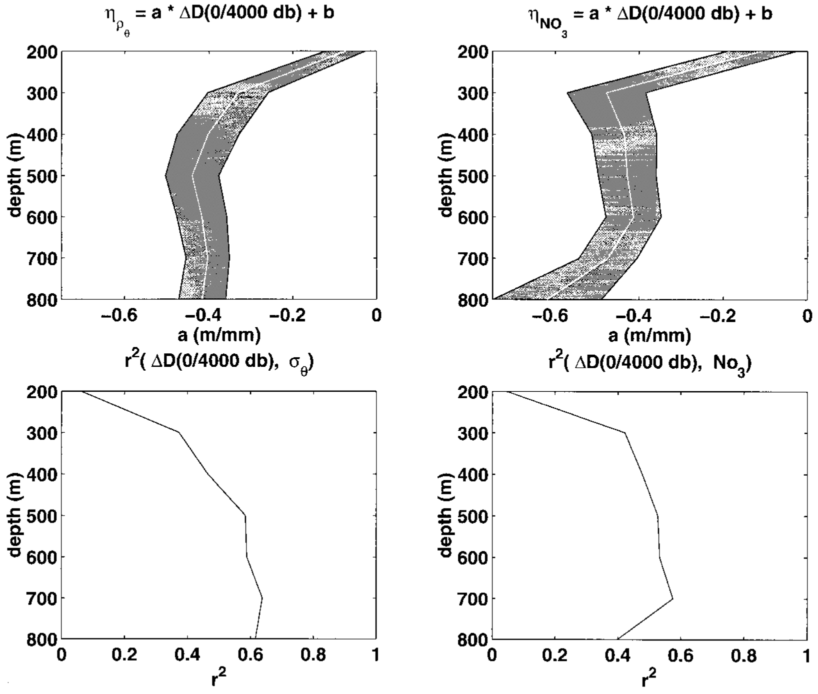

Figure 5. Linear regression slope profile (in units of meters displacement per centimeter dynamic topography) between $\Delta D(0/4000$ dbar) and the depths of (top left) isopycnal and (top right) isonutrient surfaces over the upper 1000 m at BATS. Shaded regions represent 95% confidence intervals of the slope. Values of the correlation coefficient r^2 between $\Delta D(0/4000$ dbar) and the depths of (bottom left) isopycnal and (bottom right) isonutrient surfaces. Intercepts from the linear regressions were insignificantly different from zero.

as follows. The vertical displacement of an isopycnal surface due to the passage of eddies is modeled using the empirical results presented previously; below 200 m, isopycnal displacements are related to SLA, as a 4-m upward isopleth displacement occurs for each 1-cm SLA depression (Figure 5). Above 200 m we model displacement as a decreasing linear profile that extrapolates to zero at the sea surface [i.e., $\eta_\sigma(0, t) = 0$]. Use of more complicated relationships, such as the vertical

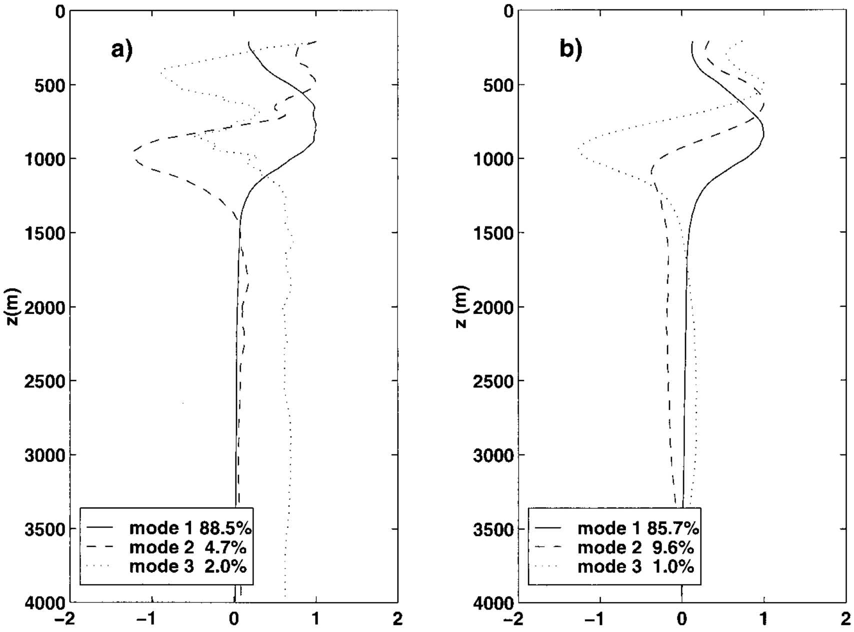

Figure 6. Vertical profile of (a) the first three empirical orthogonal function (EOF) modes and (b) the first three dynamical modes for the 7 years of BATS potential density observations analyzed. In calculating the EOF modes, data above 200 m are not used owing to difficulty in removing the seasonal heating/cooling cycle.

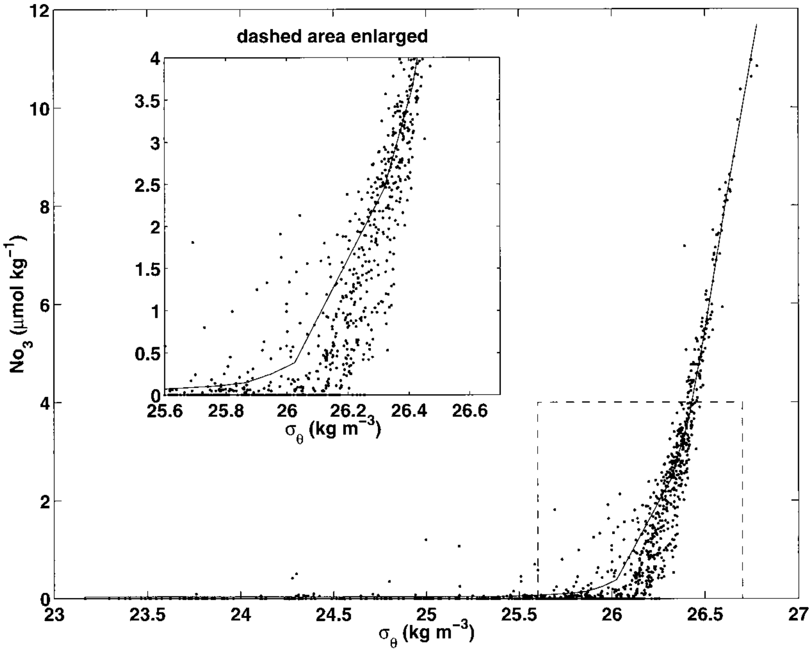

Figure 7. Nitrate–potential density relationship observed from the available BATS hydrographic data set. The inset expands the region at the base of the nitracline.

structure function for the first baroclinic mode, results in similar eddy-pumping fluxes. The displacement profile, $\eta_\sigma(z, t)$, is used to determine the displaced potential density profile, $\tilde{\sigma}_\theta(z, t)$, or

$$\tilde{\sigma}_\theta(z, t) \cong \langle \sigma_\theta(z) \rangle + \eta_\sigma(z, t) \frac{\partial \langle \sigma_\theta(z) \rangle}{\partial z} \tag{6}$$

where the mean potential density and its gradient are given in Figure 3a. The displaced nitrate profile is then calculated using the observed mean nitrate–potential density relationship (Figure 7).

Uplifting events are identified using the objectively mapped SLA time series. Relevant to the calculation of the maximum displaced nutrient profile, we need to determine the minimum SLA for a given uplifting event. An example of this event marking using the SLA time series at the BATS site is presented in Figure 8. Uplift events occur as the thermocline shallows, i.e., when the SLA becomes increasingly negative, and events end as the thermocline deepens again and the SLA increases. First- and second-derivative information in smoothed representations of the SLA time series is used to determine the end points for each individual event. The minimum SLA value is selected over this interval using the unsmoothed SLA time series. In the SLA time series at BATS (Figure 8), 18 individual upwelling events are observed, each with a mean duration of 23 days and a mean time between events of 31 days, which remains consistent with the timescale assumptions of the kinematic eddy-pumping calculation.

The deepest SLA displacements for each event are used to construct the uplifted nitrate profile. The uptake for each event is found by integrating that portion of the displaced nutrient profile above the assumed depth of the euphotic zone. For a depth of 95 m, the mean depth of the euphotic zone [*Siegel et al.*, 1995], the mean maximum displacement of the BATS SLA example is 17 m, which results in an average nutrient uptake of 0.025 mol N m^{-2} per event. The annual uptake rate is then the sum of all events divided by the time interval of the time series (1101 days). The 3-year BATS time series shown in Figure 8 results in an annual mean uptake of 0.15 mol N m^{-2} yr^{-1}. This flux estimate is likely to be low, as no extreme negative SLA values (<-20 cm) were found at BATS (Figure 2), although several features of this magnitude were observed in its vicinity (Plates 2 and 4). This suggests that longer time series will be required for calculating robust eddy statistics.

The kinematic eddy-pumping calculation is applied to the mapped SLA fields in the vicinity of the BATS site in order to extend the statistical reliability of the final estimates. This will enable more upwelling events to be captured in our rather short, 3-year available SLA time series. Objectively mapped grid locations are used in this calculation within a zonal region within ±1° latitude of the BATS latitude only when the OA expected error levels are less than 25%. The combination of SLA records for these sites results in an ~50-year time series from which we estimate eddy-pumping fluxes. There remains the caveat that each site is not truly independent of its neighbors owing to the westward propagation of mesoscale features (Plate 4a); although using data only from the three nearest T/P crossover points results in very similar flux estimates.

As expected, the eddy-pumping flux increases with the assumed depth of the euphotic zone (Figure 9). Values of the eddy-pumping flux are greater than 0.2 mol N m^{-2} yr^{-1} below 100 m and are less than 0.1 mol N m^{-2} yr^{-1} above 90 m. The regional mean eddy-pumping flux at the mean depth of the 1% photosynthetically available radiation (PAR) isolume (~95 m) is 0.184 mol N m^{-2} yr^{-1} with a standard deviation of 0.031 mol N m^{-2} yr^{-1} (Figure 9). This uncertainty estimate is determined from the ensemble of pumping flux estimates among the SLA time series used. A better estimate for the total uncertainty in this calculation would be 0.1 mol N m^{-2} yr^{-1}, which takes into account uncertainties in the procedures used to determine the maximum displaced nutrient profile and the euphotic zone depth. Direct optical measurements at BATS show the depth

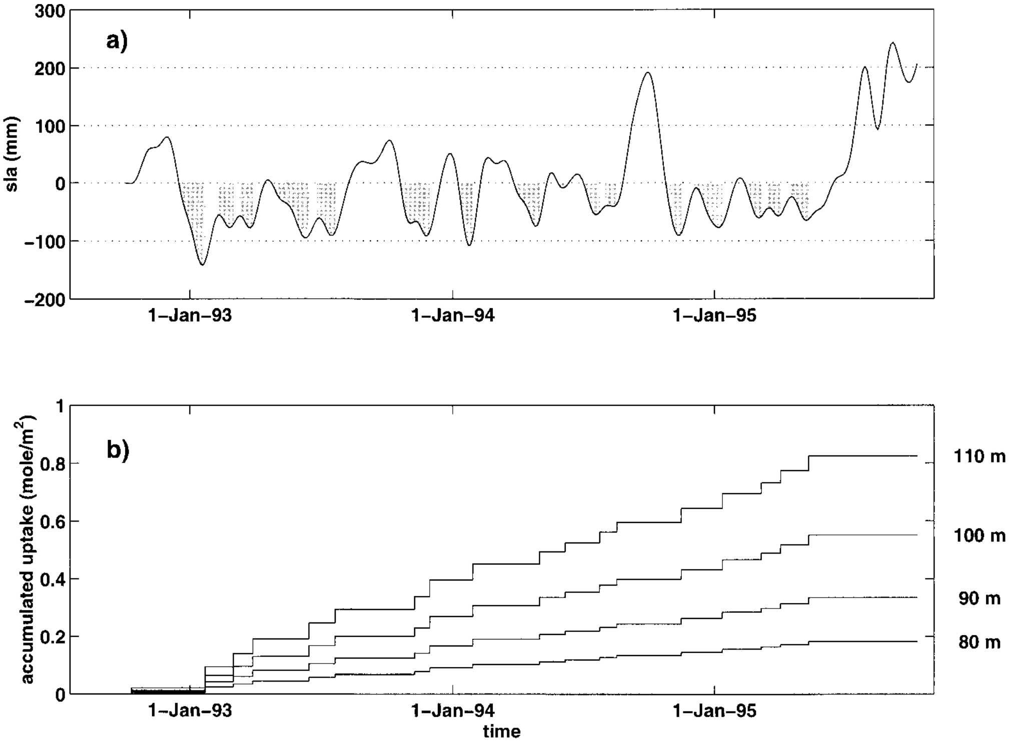

Figure 8. Example of the eddy-pumping calculation procedure using SLA estimates at the BATS site, showing (a) the time-filtered SLA time series, where the shading denotes upwelling events, and (b) the cumulative uptake for euphotic zone depths of 80, 90, 100, and 110 m in units of mol N m^{-2}. The uptake rate is determined as the cumulative uptake divided by the time interval (1101 days). A 30-day, fourth-order Butterworth filter is applied to the 3-day objectively analyzed SLA time series before gradient analyses are performed to demarcate upwelling events.

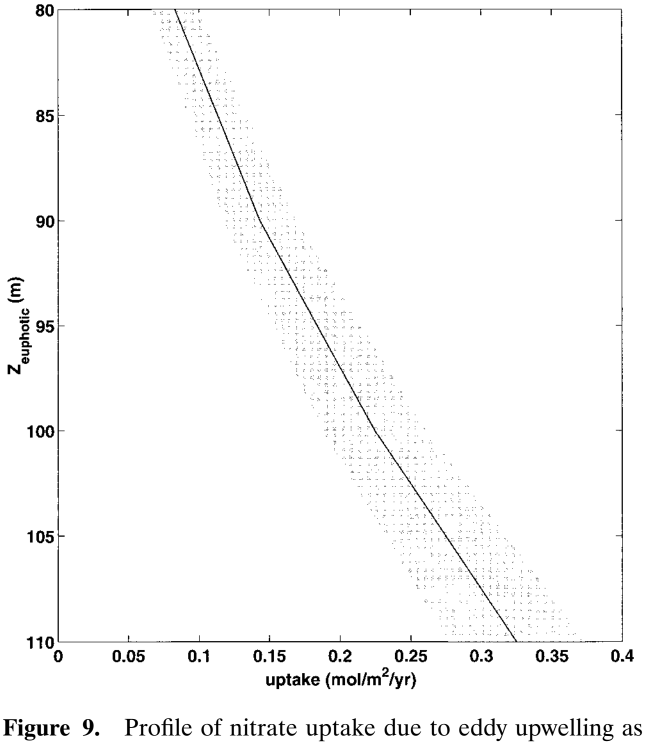

Figure 9. Profile of nitrate uptake due to eddy upwelling as a function of depth of the euphotic zone (in units of mol N m^{-2} yr^{-1}). Shaded region about the uptake profile gives the standard deviation for the various SLA time series locations used to calculate the flux.

of the 1% PAR isolume to vary about its mean depth of 94 m with a standard deviation of 12 m [*Siegel et al.*, 1995]. It should be apparent that the eddy-pumping flux will be a large portion of the total new production diagnosed for this site (Table 1).

5.2. The 18° Water Variability and Eddy Pumping

The present kinematic estimate of the eddy-pumping flux accounts only for vertical displacements due to the first vertical mode of motion. Higher vertical modes can contribute to vertical displacements in the upper 500 m (Figure 6). We have shown that the first vertical mode of variability contributes about 85% of the variance in the potential density profile and that the second mode contains 5% to 10% of the variance (Figure 6). The present calculation of eddy pumping will not account for these higher-mode displacements, as the upward displacements of the upper layers will be more than compensated by the downward displacements of the main thermocline, resulting in a positive SLA (Figure 10) [e.g., *McGillicuddy et al.*, 1999; J. D. McNeil et al., New chemical, bio-optical, and physical observations of upper ocean response to the passage of a mesoscale eddy off Bermuda, submitted to *Journal of Geophysical Research*, 1999] (hereinafter referred to as submitted manuscript, 1999). Hence the present eddy-pumping flux calculation will not account for high vertical model signals and hence is likely to be a lower bound of the total eddy-pumping flux.

One important feature expression of high vertical mode structures are variations in the thickness of the 18° water mass [e.g., *Worthington*, 1959; *Schroeder et al.*, 1959; *Jenkins*, 1982;

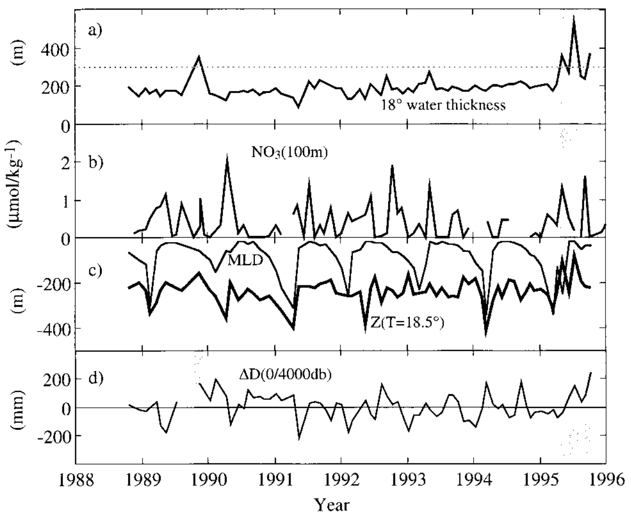

Figure 10. Time course of (a) thickness of the 18° water layer (distance between the 17.5° and 18.5°C isotherms [*Ebbesmeyer and Lindstrom*, 1986]), (b) nitrate concentration observed at 100 m, (c) the depth of the 18.5°C isotherms (thick line) and the depth of the mixed layer (thin line), and (d) the dynamic height anomaly referenced to 4000 dbar (in mm) for the available BATS hydrographic record (October 1988 to December 1995). The dotted line in Figure 10a represents a 18° water layer thickness of 300 m. The mixed layer depth is calculated using the density jump corresponding to a 0.5°C change from the sea surface temperature where the coefficient of thermal expansion is determined using surface water properties [*Siegel et al.*, 1995].

Talley and Raymer, 1982]. The thermohaline properties of the 18° water mass are remarkably stable (over interannual timescales) and are thought to be maintained by intense wintertime air-sea heat and freshwater exchanges. From the BATS hydrographic record the average depth of top of the 18° water mass (defined as the depth of the 18.5°C isotherm) is equal to 242 m (standard deviation = 54 m) and its average thickness (defined as the distance between the 17.5° and 18.5° isotherms) is 196 m (standard deviation = 60 m, Figure 10). The 18° water mass thickness varies owing to the presence of mesoscale eddies [e.g., *Talley and Raymer*, 1982; *Ebbesmeyer and Lindstrom*, 1986; *Brundage and Dugan*, 1986]. These features will be diagnosed as high vertical mode structures where a thick 18° water mass signal will correspond to a depressed main thermocline and an uplifted seasonal thermocline [*Talley and Raymer*, 1982; *Ebbesmeyer and Lindstrom*, 1986; *McGillicuddy et al.*, this issue]. A high $\Delta D(0/4000$ dbar$)$ signal is associated with the occurrence of these anomalously thick 18° water columns (Figure 10).

The 8-year-long BATS data set shows only three events where anomalously thick 18° water layers are found (October 1989, July 1995, and September 1995; Figure 10). Each of these events can be characterized by an 18° water thickness greater than 300 m, an increase in nitrate at 100 m, an upwelling of the 18.5°C isotherm, and a positive dynamic height anomaly (Figure 10). Hence these three events will not be accounted for in the present eddy-pumping calculation. The July 1995 event was observed by the Bermuda testbed mooring (BTM) array [*Dickey et al.*, 1998]. The BTM array observed chlorophyll concentrations exceeding 1 mg m^{-3} (at 60 m), which are the greatest observed in the entire BATS time series record, and peak nitrate concentrations (at 80 m) reaching ~2.5 μmol kg^{-1} [*McGillicuddy et al.*, 1998; McNeil et al., submitted manuscript, 1999]. McNeil et al. (submitted manuscript, 1999) estimate that 0.145 mol N m^{-2} of new nitrogen were required to produce the observed chlorophyll concentrations (7.3 mmol N m^{-2} d^{-1} × 20 days).

For present purposes an estimate of the eddy-pumping flux due to 18° water eddies can be made by assuming that the flux observed for the July 1995 event is typical. This assumption will likely lead to an overestimate of the annual flux due to 18° water eddies, as the July 1995 event was extremely large, resulting in both the highest chlorophyll *a* concentration (McNeil et al., submitted manuscript, 1999) and thickest 18° water layer (Figure 10) observed in the 7+-year-long BATS hydrographic record. Only three BATS cruises can be characterized as 18° water eddy events (Figure 10). As an Eulerian timescale for these events is of order 30 days, it is unlikely that many 18° water eddies were missed in the once to twice monthly sampling of the BATS site. Assuming that the three events from the 7-year BATS record truly represent the long-term mean, the annual contribution that 18° water eddies make to the nitrogen budget off Bermuda will be less than 0.06 mol N m^{-2} yr^{-1}. The uncertainty bounds on this estimate are undoubtedly large (roughly 50% of the estimate), but this still indicates that new nutrient supply due to 18° water eddies is significantly smaller than the low-mode eddy-pumping flux calculated previously.

5.3. Vertical Nutrient Transport by Turbulent Diffusion

Eddy pumping is one of many physical mechanisms capable of transporting nutrients into the euphotic zone. Small-scale diffusive processes acting either across isopycnal surfaces or along tilted isopycnal surfaces provide two additional mechanisms that can transport new nutrients into the euphotic zone. The vertical component of the cross-isopycnal, or diapycnal, flux of nutrients, F_{vd}, is equal to

$$F_{vd} = -K_d \frac{\partial N}{\partial x_d} \cos\theta \cong -K_d \frac{\partial N}{\partial z} \tag{7}$$

where K_d is the diapycnal turbulent diffusion coefficient, N is the nutrient concentration, x_d represents the diapycnal direction, z is the vertical direction, and θ is the angle between the isopycnal and a horizontal surface. As the isopycnals are nearly horizontal ($\cos\theta \cong 1$), rates of diapycnal nutrient flux can easily be calculated using the vertical gradient of the mean nitrate profile (Figure 3b) and an estimate of diapycnal diffusivity K_d. Typical values for the diapycnal diffusivity are of order 10^{-5} m^2 s^{-1} [e.g., *Gregg*, 1987; *Ledwell et al.*, 1993], while the "abyssal recipes" value of 10^{-4} m^2 s^{-1} [*Munk*, 1966] provides a useful upper bound. Using the abyssal recipes value, the mean diapycnal nutrient flux at 95 m is 0.03 mol N m^{-2} yr^{-1}, which is a small fraction of the eddy-pumping flux. Application of a realistic value for K_d ($\sim 10^{-5}$ m^2 s^{-1}) results in a much smaller diapycnal flux (≤ 0.005 mol N m^{-2} yr^{-1}). It seems apparent that diapycnal diffusion will not be an important process transporting nutrients into the euphotic zone. We will quantify the contribution of diapycnal diffusion to the new nitrogen budget as 0.015 mol N m^{-2} yr^{-1} (with an uncertainty of 0.015 mol N m^{-2} yr^{-1}) to account for uncertainties in K_d.

Vertical transport due to eddy diffusive mixing along sloping isopycnals is another mechanism that can provide a significant vertical transport of nutrients [e.g., *Hayward*, 1987; *Jenkins*, 1988; *Washburn et al*., 1989, 1991]. The upward vertical component of the isopycnal diffusive flux, $F_{vi}(\uparrow)$, can be represented as

$$F_{vi}(\uparrow) = -\frac{1}{2} K_i \frac{\partial N}{\partial x_i} \sin\theta \qquad (8)$$

where K_i is the isopycnal eddy diffusion coefficient, x_i represents the isopycnal direction, and the factor of 1/2 reflects that about half of the time, an isopycnal surface is depressed from its mean position rather than the upwelling case, where net nutrient transport occurs. Estimation of $F_{vi}(\uparrow)$ is problematic, as it requires the determination of the isopycnal slope (or θ), the isopycnal nutrient gradient, and the isopycnal eddy diffusion coefficient. Each of these terms contains a large degree of uncertainty, which will preclude the determination of $F_{vi}(\uparrow)$ as a function of time and space. Hence we will only attempt to derive scale estimates for the vertical transport across the base of the euphotic zone caused by mixing along sloping isopycnals.

Estimates of the slope of an isopycnal surface can be made knowing the local geostrophic currents. That is, the eddy component of the geostrophic current is related to the slope of the sea surface [$u_E = (-g/f)\partial\mathrm{SLA}/\partial y$ and $v_E = (g/f)\partial\mathrm{SLA}/\partial x$], while an isopycnal's displacement can be estimated using the empirical mapping provided in Figure 5. For the zonal region, ±1° latitude about the BATS site (31° to 33°N), the mean speed of the geostrophic current at the sea surface is equal to $0.132\ \mathrm{m\ s^{-1}}$. This is equivalent to a typical magnitude for the SLA gradient of 1.0×10^{-6} (1-mm sea level tilt per kilometer). The corresponding isopycnal surface slope at 200 m is ~4.1 m displacement per kilometer, and at a depth of 100 m this slope is $\sim 2.1 \times 10^{-3}$.

In determining the eddy-pumping flux, we assume that the nutrient concentration on an isopycnal surface is described by the mean potential density–nutrient concentration relationship (Figure 7), unless the surface has been uplifted into the euphotic zone where it is utilized. Hence an isopycnal nutrient gradient will exist across the base of the euphotic zone, where the nutrient concentration difference can be estimated knowing only the isopycnal's potential density. In the following we assume that the upwelled isopycnal has a nitrate value of 2.5 $\mu\mathrm{mol\ N\ kg^{-1}}$, which has been uplifted from a depth of ~200 m (Figure 3b). The horizontal length scale over which this gradient occurs is much harder to estimate. Natural length scales that enter the problem are the radial extent of an eddy (~100 km) and the depth scale over which the ambient light field is attenuated. The vertical gradient of the available light field regulates the uptake of nitrate and creates the isopycnal nutrient gradient. Combining an e-folding depth scale for the ambient light field (~20 m) with the scale estimate for the isopycnal slope at 100 m, the resulting horizontal length scale is ~10 km. In the following we will make scale estimates using both length scales.

The selection of an appropriate isopycnal mixing coefficient is the last important step in determining the vertical component of isopycnal mixing. We want to quantify the mixing that occurs along sloping isopycnal surfaces on the side of a mesoscale eddy. Hence the length scale over which isopycnal mixing occurs will be small (≤10 km). Using the diffusion diagrams of *Okubo* [1971], estimates of horizontal diffusivity are approximately 8 and 100 $\mathrm{m^2\ s^{-1}}$ for length scales of 10 and 100 km, respectively. These values are likely to be severe overestimates because the measurements used to derive the diffusion diagrams were observations of dye dispersion on lake surfaces [*Okubo*, 1971], and many other processes in addition to isopycnal mixing can disperse water parcels, increasing estimates of diffusivity above those expected within the seasonal pycnocline. Direct observations of isopycnal mixing using a purposeful tracer field on spatial scales of several tens of kilometers to ~100 km resulted in a K_i estimate of $\sim 0.1\ \mathrm{m^2\ s^{-1}}$ [*Ledwell et al*., 1993]. Using the likely overestimates of K_i from *Okubo*'s [1971] diffusion diagrams, the resulting scale estimates for the vertical component of isopycnal mixing at the base of the euphotic zone are 0.068 and 0.085 $\mathrm{mol\ N\ m^{-2}\ yr^{-1}}$ for length scales of 10 and 100 km, respectively. Using a more reasonable upper bound for K_i, such as $1\ \mathrm{m^2\ s^{-1}}$, the resulting fluxes are much smaller ($\leq 0.008\ \mathrm{mol\ N\ m^{-2}\ yr^{-1}}$). Any smaller value of K_i will result in a negligible flux. Similar to the conclusions drawn above for diapycnal diffusive fluxes, isopycnal fluxes become an important component of the new nitrogen budget only when unreasonably large estimates for the diffusivity are used. For present purposes, we will assume that the scale estimate for the vertical flux due to isopycnal mixing is $0.03\ \mathrm{mol\ N\ m^{-2}\ yr^{-1}}$ (with an uncertainty of $0.03\ \mathrm{mol\ N\ m^{-2}\ yr^{-1}}$), which is likely to be an overestimate for this process. However, it should be apparent that diffusive processes will be a small component of the nutrient supply budget at this site.

5.4. Vertical Nutrient Transport by Wintertime Convection

Wintertime convection has long been known to be the dominant process bringing new nutrients into the euphotic zone of the northern Sargasso Sea [e.g., *Riley*, 1957; *Menzel and Ryther*, 1961; *Glover and Brewer*, 1988; *Siegel et al*., 1990, 1995; *Michaels et al*., 1994b; *Doney et al*., 1996; *Michaels and Knap*, 1996]. Cold, dry winter storms create deep mixed layers due to their intense air-sea buoyancy exchanges. New nutrients are then entrained into the mixed layer as part of this convective deepening process. A spring bloom will occur once the mixed layer shallows to less than the euphotic zone depth [*Sverdrup*, 1953]. This springtime incorporation of nutrients into the euphotic zone food web represents a new nitrogen supply.

In order to estimate the wintertime convective input of new nutrients, we assume that winter mixing will homogenize the water column to the depth of the deepest mixed layer. The mean concentration of the mixed nutrient profile is calculated using the nitrate inventory in the layer bounded by the outcropped isopycnal and the sea surface for the 6-month period prior to the deep mixing event. The depth of the maximum observed mixed layer depth D_{max} and the mean and maximum inventories of mixed nitrate are given in Table 2. We use the maximum inventory ($\int \mathrm{NO_{3\ max}}$) in our calculation of convective nutrient supply in an attempt to account for uptake that may occur during the mixed layer deepening process. Incorporation of new nitrate is assumed to occur only within the euphotic zone ($D_{\mathrm{eu}} = 95$ m); hence we estimate the convective input of new nutrients as $\int \mathrm{NO_{3\ max}}\, D_{\mathrm{eu}}/D_{\mathrm{max}}$ (Table 2). The mean annual transport is equal to $0.17\ \mathrm{mol\ N\ m^{-2}\ yr^{-1}}$ (standard deviation = $0.05\ \mathrm{mol\ N\ m^{-2}\ yr^{-1}}$), which is consistent with previous estimates of this process (Table 2). The 1990 mixing year was not used in calculating the mean annual transport, as it appears that the deep mixing event for that year was not sampled in the hydrographic record. The annual flux presented is likely to be an underestimate, as uptake of new nitrogen can occur before the spring bloom has initiated, enabling nutrient concentrations from below the euphotic zone

Table 2. New Nitrogen Transport due to Wintertime Convection

Mixing Year	Mixed Layer Depth, m	Typical $\int NO_3$, mol N m^{-2}	Peak $\int NO_3$, mol N m^{-2}	Convective Flux, mol N m^{-2} yr^{-1}
1989	302	0.45	0.65	0.21
1990	154	0.03	0.08	0.06
1991	314	0.37	0.60	0.18
1992	258	0.22	0.34	0.13
1993	230	0.19	0.29	0.12
1994	342	0.53	0.81	0.23
1995	344	0.41	0.63	0.17
Mean*	298	0.36	0.56	0.17 (0.05)

Reference	Method	Convective Flux, mol N m^{-2} yr^{-1}
Michaels et al. [1994b]†	BATS hydrography	0.17
Glover and Brewer [1988]	NO_3 and MLD climatology	0.30
Doney et al. [1996]‡	ecosystem model of BATS	0.24

Convective flux is calculated assuming that the maximum integrated nitrate concentration is homogenized within the deepest mixed layer and then utilized within euphotic zone (taken to be 95 m). Value in parentheses is the standard deviation.

*Data from 1990 are not used in making the mean owing to the very shallow mixed layer depth (MLD) observed in the BATS data set.

†Estimate is given for mixing year 1989 only.

‡Estimate is given for a depth of 140 m.

to be utilized [e.g., *Dugdale and Goering*, 1967; *Siegel et al.*, 1990]. There is also fairly good agreement between the present estimates and previous results [e.g., *Glover and Brewer*, 1988; *Doney et al.*, 1996].

5.5. Nutrient Supply Budget at BATS

To complete our synthesis of the annual new nutrient supply budget at the BATS site, a few additional flux determinations are required. These include the new nitrogen fluxes due to the convergence of Ekman transports and atmospheric deposition. *Williams and Follows* [1998] have determined the climatological role of direct, wind-driven transport of nutrients in the North Atlantic Ocean. They find that the convergence of Ekman transports in the Sargasso Sea acts as a source of new nutrients owing to advection of nutrients from the north. Their annual flux of new nutrients at BATS due to Ekman transport is 0.03 mol N m^{-2} yr^{-1} with an uncertainty of 0.01 mol N m^{-2} yr^{-1} (M. Follows, personal communication, 1997). Finally, atmospheric deposition of nitrogen, both as inorganic and organic compounds, has been shown to be a minor contributor to the new nitrogen supply budget off the Sargasso Sea [e.g., *Knap et al.*, 1986; *Michaels et al.*, 1993; *Prospero et al.*, 1996]. Annual wet deposition flux estimates for all NO_x and NH_y species are of order 0.01 mol N m^{-2} yr^{-1} or less (depending upon which Bermuda deposition data set is evaluated), while the organic nitrogen flux is of the same order [*Prospero et al.*, 1996]. The dry deposition flux of nitrogen compounds is not as well known but, again, should be something less than 0.01 mol N m^{-2} yr^{-1} [*Prospero et al.*, 1996]. Hence an upper bound for the new nitrogen supply due to atmospheric deposition is 0.03 mol N m^{-2} yr^{-1} with an uncertainty of roughly 0.01 mol N m^{-2} yr^{-1}.

With these final new nutrient supply estimates in hand, we can now complete the new nitrogen supply budget for BATS (Table 3). The dominant terms are the sum of the eddy-pumping fluxes (a total of 0.24 mol N m^{-2} yr^{-1}) and the winter convective flux (at least 0.17 mol N m^{-2} yr^{-1}). Diffusive mixing, large-scale Ekman convergence, and atmospheric deposition are less important to the total budget (an upper bound estimate of 0.11 mol N m^{-2} yr^{-1}). Adding up all of the components, the total new nitrogen supply is 0.51 mol N m^{-2} yr^{-1} with an uncertainty of roughly 0.15 mol N m^{-2} yr^{-1}. This uncertainty should be a good upper bound, considering the character of the assumptions applied. The annual estimate of total new nitrogen supply assumes that those flux components that are likely to be overestimated (18° water input and diffusive transports) are balanced by those terms that may be underestimated (winter convection). The mean new nutrient supply is nearly identical to the mean of the geochemical estimates of new production made near the island of Bermuda (Table 3).

The nutrient budget calculations presented here are consistent with those of *McGillicuddy and Robinson* [1997]. The MR97 estimate of eddy-induced transport (0.36 ± 0.1 mol N m^{-2} yr^{-1}) included diapycnal diffusion. Hence the appropriate value to compare with the MR97 results is the sum of eddy-driven and diffusive transports, ~0.30 mol N m^{-2} yr^{-1}. It must be pointed out that the present estimates of eddy transport include a contribution of 0.06 mol N m^{-2} yr^{-1} from 18° water eddies. It is not yet clear to what extent features of this type are represented in the MR97 calculations, and this diagnosis is the subject of future work. Notwithstanding that issue, these two independent flux estimates are clearly in agreement within the expected uncertainty bounds.

The present calculations have closed effectively the new nitrogen supply budget at BATS. This, by itself, presents an interesting quandary. The BATS total carbon inventory shows

Table 3. New Nutrient Transport Estimates for BATS

	Annual Flux, mol N m^{-2} yr^{-1}	Uncertainty, mol N m^{-2} yr^{-1}	Notes
Diapycnal diffusion	0.015	0.015	likely overestimate
Isopycnal diffusion	0.03	0.03	likely overestimate
Eddy pumping using SLA	0.18	0.10	statistical estimate from altimetry and hydrography
Eddy pumping by 18° water	0.06	0.03	likely overestimate, assumes 1995 event* is typical
Winter convection	0.17	0.05	probable lower bound
Large-scale Ekman pumping	0.03	0.01	*Williams & Follows* [1998]
Atmospheric deposition	0.03	0.01	likely overestimate *Prospero et al.* [1996]
Total nutrient flux	0.51	0.15	
Annual new production	0.50	0.14	

*See McNeil et al. (submitted manuscript, 1999).

a significant, summertime drawdown in the absence of any significant export or air-sea exchange or obvious supply of new nutrients [*Michaels et al*., 1994a]. Further, the dissolved nutrient stoichiometeric record at BATS shows nitrate to phosphate ratios exceeding Redfield values for the upper 700 m of the water column [e.g., *Michaels et al*., 1994b]. Both of these results point toward nitrogen fixation, the conversion of dissolved dinitrogen gas to usable forms of nitrogen, as an important contributor to the new nitrogen budget [e.g., *Michaels et al*., 1996; *Gruber and Sarmiento*, 1997]. By evaluating the concentration of excess inorganic nitrogen (above Redfield) on isopycnal surfaces and radiotracer-determined isopycnal residence times, *Michaels et al*. [1996] estimated that nitrogen fixation rates should be between 0.19 and 0.32 mol N m^{-2} yr^{-1}. *Gruber and Sarmiento* [1997] used a slightly different approach and estimated a nitrogen fixation rate of 0.07 mol N m^{-2} yr^{-1} for the BATS site. On the other hand, direct determinations of nitrogen fixation by *Trichodesmium*, the dominant nitrogen fixer for this region, have been less than 0.01 mol N m^{-2} yr^{-1} for the BATS site [e.g., *Lipschultz and Owens*, 1996]. This biologically mediated source of new nitrogen is not accounted in the present nutrient supply budget.

Eddy pumping does not provide a convenient explanation for the summertime drawdown of total carbon concentrations or the pronounced non-Redfield stoichiometry observed at BATS. During an eddy upwelling event the upwelled waters also contain dissolved inorganic carbon (DIC) concentrations, which are incorporated as the new nutrients are utilized. Hence it seems unlikely that eddy pumping affects the observed DIC drawdown and the eddy upwelling flux will only act to exacerbate this carbon imbalance [*McGillicuddy et al*., 1998]. Further, eddy pumping does not provide a mechanism that will alter nutrient concentrations from a Redfield balance. In fact, the present eddy-pumping calculation assumes implicitly that the nutrient dynamics will follow Redfield proportions. If the higher estimates of N_2 fixation prove to be correct, the combined new nutrient fluxes will exceed typical geochemical estimates of new production (Table 1). The resolution of this question is beyond the scope of the present contribution and will only be accomplished through the direct determination of the rates of nutrient supply and ecosystem utilization on appropriate space and timescales.

5.6. Particle Transport, Mesoscale Eddies, and Eddy-Pumping Fluxes

The present calculation of the eddy-induced flux and its role in the incorporation of new nutrients makes an important assumption concerning how water parcels are transported by mesoscale motions. If water parcels remain within the interior of an eddy for a "long" time, the present calculation will estimate the true eddy-pumping flux. Whereas if these water parcels disperse "quickly" from the eddy interior, the present results should be an underestimate of the actual eddy-pumping flux. The words "long" and "quickly" here refer to dispersal times relative to the timescales for the uplift, uptake, and remineralization. This quandary raises the age-old question of particle transport by turbulence versus wave motions. That is, are the mesoscale motions turbulent, which will stir and disperse water parcels through an eddy's lifetime, or are they planetary waves, which will simply displace isopycnal surfaces as they propagate through a region? The resolution of this issue is critical for the proper interpretation of the eddy-pumping calculations.

Evidence for both wave and turbulent characters for the observed motions can be deduced from present results and the literature. For example, the observed mesoscale features propagate to the west with phase speeds that are about twice the maximum speed of the fastest dynamical mode (Plate 4; see also *Chelton and Schlax* [1996]). *Killworth et al*. [1997] have shown that these signals are consistent with Doppler shifting of linear Rossby waves by the baroclinic component of the mean flow. An annual period SLA signal is also observed (Plate 4). This low-frequency signal has been shown to be driven by linear, wind-forced Rossby wave motions [*Polito and Cornillon*, 1997]. Hence there is some consistency between the present SLA observations and linear wave theory.

However, it does not seem likely that the present mesoscale features are simply planetary waves. For example, westward propagation is not only a characteristic of linear Rossby waves, as isolated eddies on a β plane also propagate to the west [e.g., *Flierl*, 1987]. This picture of a dynamic mesoscale eddy field appears compatible with observations. The planform structures of the SLA fields show many, closed circulation eddies that interact, merge, and evolve over time as they propagate to the west (Plates 2 and 4; see http://www.icess.ucsb.edu/~davey/TP_BATS/BATS_sla_currents.mpg). These motions are surely not linear waves. Analysis of SOFAR float trajectories illustrates many examples where floats are trapped within mesoscale features for a little as a month and for as long as a year [*Richardson*, 1993]. Looping trajectories comprise roughly 25% of the total number of the 700-m float days observed in the Sargasso Sea. Nearly 60% of these looping trajectories are cyclonic with radial scales of 90 to 100 km. These scale determinations are similar to those diagnosed here using the altimetric SLA fields (although the isobaric floats are drogued at 700 m).

In all, the observed mesoscale features are consistent with present concepts of an interacting, dynamic mesoscale eddy field rather than the simple propagation of a train of linear planetary waves. Relevant to the present calculations, knowledge of the timescales that characterize water parcel retention and cyclonic eddy formation is required. These Lagrangian timescales are likely to be much longer than the Eulerian times (~30 days) that characterize the passage of a single event (Plate 4 and Figures 2 and 8). Clearly, more research is required; but the resolution of this issue is important for developing a predictive understanding of the role of eddies in the ocean's biogeochemical cycles.

6. Summary and Conclusions

An analysis of satellite altimetry and hydrographic observations is used to characterize the mesoscale eddy field about the BATS site and to estimate the new nitrogen supply budget. The observed sea level anomaly field is dominated by the occurrence of westward propagating features with SLA signatures as large as 25 cm, propagation speeds of ~5 cm s^{-1}, Eulerian temporal scales of roughly a month, lifetimes of several months (or more), and spatial scales of 100 to 200 km. Estimates of dynamic height anomaly from the hydrographic observations are well correlated with satellite SLA, and at least 85% of the observed dynamic height variability is associated with the first baroclinic mode of motion. This allows us to use the satellite SLA fields to estimate a flux of nutrients into the euphotic zone due to the eddy-pumping mechanism of 0.24 mol N m^{-2} yr^{-1}. This flux is much larger than any estimate of diffusive flux, indicating that eddy pumping is the dominant physical mechanism transporting nutrients into the euphotic zone of the Sargasso Sea during the summer. Winter convection transports roughly the same amount of new nutrients into the euphotic zone. The sum of the new nitrate transports provides ~0.5 mol N m^{-2} yr^{-1}, which effectively balances geochemical estimates of the annual new production for BATS.

Although we have suggested closure of the new nitrogen budget for the Sargasso Sea, many outstanding questions remain. For example, the proper interpretation of the present kinematic eddy-pumping flux calculations requires knowledge of the residence time for water parcels in a mesoscale feature and cyclonic eddy formation relative to the appropriate biogeochemical timescales. A detailed understanding of these purely physical oceanographic questions needs to be achieved. Another question pertains to the role of nitrogen fixation in the new nitrogen budget at BATS. The sum of the present quantification of the eddy-pumping flux with the higher estimates of nitrogen fixation result in a new nitrogen supply budget that is too large compared with the various geochemical estimates (except for the recent estimate of 0.7 ± 0.2 mol N m^{-2} yr^{-1} made by *Jenkins* [1998]). The irony of this situation is that throughout the late 1980s and 1990s, investigators were trying to find enough nitrogen to balance the geochemical rates. Now there appears to be too much nitrogen. Rectifying this situation is critical if we are to understand and quantify rates of new production for the open sea.

The case for eddy-induced nutrient supply in the Sargasso Sea seems compelling; however, the role of mesoscale processes in basin-scale biogeochemical budgets is far from clear. The regional studies described herein have attempted to examine the ramifications of thermocline displacements and associated perturbations to the mean nutrient profile. Understanding how this profile is maintained will almost certainly require treatment of the larger-scale circulation, both in terms of its time mean and eddying components [e.g., *Jenkins*, 1998]. Establishing the functionality of the eddy upwelling mechanism in its basin-scale context should provide a means for parameterization of the resulting nutrient flux in coarse resolution models. Likely elements of such a parameterization include the root-mean-square isopycnal displacements at the base of the euphotic zone, the ratio of positive to negative perturbations, the mean nutrient gradient, and measures of Lagrangian timescales for the eddy field. Many of the above quantities can be determined from a combination of satellite and hydrographic information as was done here. However, this work must be performed before we are to understand thoroughly the importance of eddy pumping globally.

Appendix: Calculation of Space-Time Correlation Model

Our goal is to estimate the best possible mesoscale fields of sea level anomaly (SLA) along with their associated mapping errors. Our intent is to keep track of the expected error from the objective analysis procedure (OA); hence we are not requiring the error fields to be spatially and temporally uniform [e.g., *Greenslade et al.*, 1997]. The expected error fields are used to assign weights to each analysis point in the calculations made herein.

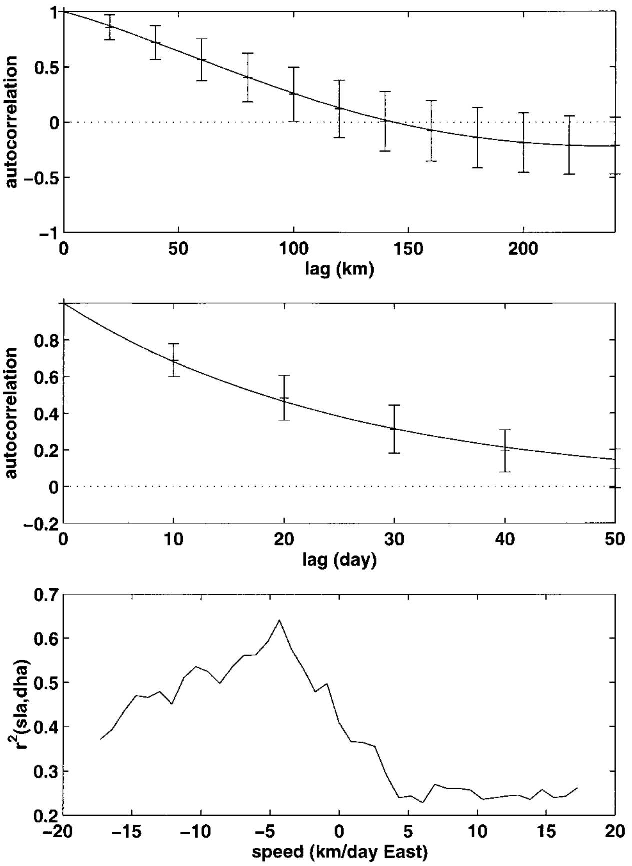

Figure A1. TOPEX/POSEIDON (top) along-track autocorrelation function and (middle) crossover temporal autocorrelation function for the region about BATS. Error bars represent standard deviation envelopes for the altimetry data sets used, and solid lines are the final analytical models used (equations (A1a) and (A1b)). (bottom) Values of the correlation coefficient r^2 between $\Delta D(0/4000$ dbar) and the objectively analyzed SLA for the BATS site as a function of the assumed phase speed c.

Development of an OA procedure for regularizing randomly distributed observations requires knowledge of the space-time correlation distribution for the measurement field [e.g., *Thiébaux and Pedder*, 1987; *Carter and Robinson*, 1987]. The correlation model used was determined using T/P cycles 2 through 114 (3 years of data) for the region about the BATS site. Third-order trends were removed in time (from the 3-year time series) and in space (from the ~1500-km-long along-track data). Depiction of the radial and temporal autocorrelation functions is shown in Figure A1, top and middle, respectively. The resulting autocorrelation functions were modeled as

$$C(r) = \exp(-r/175)\cos(2\pi r/575) \qquad \text{(A1a)}$$

$$C(\Delta t) = \exp(-|\Delta t|/26) \qquad \text{(A1b)}$$

where r is equal to $(\Delta x^2 + \Delta y^2)^{1/2}$ in units of kilometers, Δx is distance between observations in the zonal direction, Δy is distance in the meridional direction, and Δt is in units of days. These functions are shown as the solid lines in Figure A1. Analyses showed no apparent zonal-meridional asymmetry in the correlation model. The present results are consistent with the correlation analysis done by *Stammer* [1997] using a global version of the T/P data set.

In the Sargasso Sea, mesoscale features are generally observed to migrate to the west (Plate 4), and this statistical tendency must be accounted for in the OA correlation model [e.g., *Thiébaux and Pedder*, 1987; *Carter and Robinson*, 1987]. This is achieved by recasting the radial coordinate r to include the effects of westward phase propagation, or

$$R = \sqrt{(\Delta x - c\Delta t)^2 + \Delta y^2} \tag{A2}$$

where R is the new radial coordinate in units of kilometers and c is the phase speed of westward propagation. The value for c is determined by comparing the BATS dynamic height anomaly time series, $\Delta D(0/4000 \text{ dbar})$, with the T/P SLA estimates objectively mapped to the same location. An example of this comparison is shown in Figure A1, bottom, which shows the percent variance in $\Delta D(0/4000 \text{ dbar})$ explained by the SLA estimates as a function of the assumed value of the phase speed c. The best comparison comes when the phase speed is equal to 5 cm s^{-1}, which is similar to estimates found in other studies [e.g., *Richman et al.*, 1977]. The final correlation model used is

$$C(R, \Delta t) = \exp(-R/175)\cos(2\pi R/575)\exp(-|\Delta t|/26) \tag{A3}$$

In the present application the T/P observational error was assumed to be 5% of the observed variance, the ERS 1 and ERS 2 SLA variance was taken to be 15% of the observed variance, and all observational errors were assumed to be uncorrelated.

Acknowledgments. The authors would like acknowledge support from NSF and NASA under the U.S. JGOFS Synthesis and Modeling Program, the SeaWiFS Science Team, and the NSCAT science team. The present analyses would not have been possible without the hard work and dedication of the scientists and technicians of the U.S. JGOFS BATS program, which is supported by NSF, and the TOPEX/POSEIDON program. Discussions/comments with/from Marlon Lewis, Tony Michaels, Joe McNeil, Joel Michaelsen, Jim Yoder, Paulo Polito, Jim Frew, Norm Nelson, Tommy Dickey, and Scott Doney were helpful for the presentation of the ideas made in the manuscript.

References

Altabet, M. A., A time-series study of the vertical structure of nitrogen and particle dynamics in the Sargasso Sea, *Limnol. Oceanogr.*, *34*, 1185–1201, 1989.

Archiving, Validation, and Interpretation of Satellite Data in Oceanography (AVISO), AVISO handbook: Sea level anomaly files, *Publ. AVI-NT-001-312-CN*, 21st ed., 24 pp., Cent. Natl. d'Etudes Spatiales, Toulouse, France, 1997.

Bernada, R., Merged GDR (TOPEX/Poseidon) Users Handbook, version 1, *Tech. Rep. 11007*, Jet Propul. Lab., Pasadena, Calif., 1993.

Brundage, W. L., and J. P. Dugan, Observations of an anticyclonic eddy of 18C water in the Sargasso Sea, *J. Phys. Oceanogr.*, *16*, 717–727, 1986.

Buesseler, K. O., Do upper-ocean sediment traps provide an accurate record of particle flux?, *Nature*, *353*, 420–423, 1992.

Buesseler, K. O., Decoupling of production and particulate export in the surface ocean, *Global Biogeochem. Cycles*, *12*, 297–310, 1998.

Buesseler, K. O., A. F. Michaels, D. A. Siegel, and A. H. Knap, A 3-D calibration of sediment traps using Thorium scavenging, *Global Biogeochem. Cycles*, *8*, 179–193, 1994.

Carter, E. F., and A. R. Robinson, Analysis methods for the estimation of oceanic fields, *J. Atmos. Oceanic Technol.*, *4*, 49–74, 1987.

Chelton, D. B., and M. G. Schlax, Global observations of oceanic Rossby waves, *Science*, *272*, 234–238, 1996.

Dickey, T., et al., Seasonal variability of bio-optical and physical properties in the Sargasso Sea, *J. Geophys. Res.*, *98*, 865–898, 1993.

Dickey, T., et al., Preliminary results from the Bermuda testbed mooring program, *Deep Sea Res.*, *Part I*, *45*, 771–794, 1998.

Doney, S. C., D. M. Glover, and R. G. Najjar, A new coupled, one-dimensional biological-physical model of the upper ocean: Applications to the JGOFS Bermuda-Atlantic Time-series Study (BATS) site, *Deep Sea Res.*, *Part II*, *43*, 591–624, 1996.

Ducklow, H. W., et al., Dissolved organic carbon as a component of the biological pump in the North Atlantic Ocean, *Philos. Trans. R. Soc. London*, *Ser. B*, *348*, 161–167, 1995.

Dugdale, R. C., and J. J. Goering, Uptake of new and regenerated forms of nitrogen in primary productivity, *Limnol. Oceanogr.*, *12*, 196–206, 1967.

Eanes, R., and S. Bettadpur, The CSR 3.0 global ocean tide model, *Tech. Memo. CSR-TM-95-06*, Cent. for Space Res., Univ. of Tex., Austin, 1995.

Ebbesmeyer, C. C., and E. J. Lindstrom, Structure of 18°C water observed during the POLYMODE local dynamics experiment, *J. Phys. Oceanogr.*, *16*, 443–453, 1986.

Eppley, R. W., and B. J. Peterson, Particulate organic matter flux and planktonic new production in the deep ocean, *Nature*, *282*, 677–680, 1979.

Falkowski, P. G., D. Ziemann, Z. Kolber, and P. K. Bienfang, Role of eddy pumping in enhancing primary production, *Nature*, *352*, 55–58, 1991.

Flierl, G. R., Isolated eddy models in geophysics, *Annu. Rev. Fluid Mech.*, *19*, 493–530, 1987.

Flierl, G. R., and C. S. Davis, Biological effects of Gulf Stream meandering, *J. Mar. Res.*, *51*, 529–560, 1993.

Frankignoul, C., Low-frequency temperature fluctuations off Bermuda, *J. Geophys. Res.*, *86*, 6522–6528, 1981.

Fu, L. L., E. J. Christensen, C. A. Yamarone Jr., M. Lefebvre, Y. Menard, M. Dorrer, and P. S. Scudier, TOPEX/POSEIDON mission overview, *J. Geophys. Res.*, *99*, 24,369–24,381, 1994.

Gavart, M., and P. DeMey, Isopycnal EOFs in the Azores Current Region: A statistical tool for dynamical analysis and data assimilation, *J. Phys. Oceanogr.*, *27*, 2146–2157, 1997.

Gill, A. E., *Atmosphere-Ocean Dynamics*, 662 pp., Academic, San Diego, Calif., 1982.

Glover, D. M., and P. G. Brewer, Estimates of winter-time mixed layer nutrient concentrations in the North Atlantic, *Deep Sea Res.*, *Part A*, *35*, 1525–1546, 1988.

Greenslade, D. J. M., D. B. Chelton, and M. G. Schlax, The midlatitude resolution capability of sea level fields constructed from single and multiple satellite altimeter datasets, *J. Atmos. Oceanic Technol.*, *14*, 849–870, 1997.

Gregg, M. C., Diapycnal mixing in the thermocline: A review, *J. Geophys. Res.*, *92*, 5249–5286, 1987.

Gruber, N., and J. L. Sarmiento, Global patterns of nitrogen fixation and denitrification, *Global Biogeochem. Cycles*, *11*, 235–266, 1997.

Gust, G., et al., Particle fluxes and moving fluids–Experience from synchronous trap collections in the Sargasso Sea, *Deep Sea Res.*, *Part A*, *39*, 1071–1083, 1992.

Haury, L. R., J. A. McGowan, and P. H. Wiebe, Patterns and processes in the time-space scales of plankton distributions, in *Spatial Patterns in Plankton Communities*, edited by J. H. Steele, pp. 277–327, Plenum, New York, 1978.

Hayward, T. L., The nutrient distribution and primary production in the central North Pacific, *Deep Sea Res.*, *Part A*, *34*, 1593–1627, 1987.

Jenkins, W. J., On the climate of a subtropical ocean gyre: Decade timescale variations in water mass renewal in the Sargasso Sea, *J. Mar. Res.*, *40*, suppl., 265–290, 1982.

Jenkins, W. J., Nitrate flux into the euphotic zone near Bermuda, *Nature*, *331*, 521–522, 1988.

Jenkins, W. J., Studying subtropical thermocline ventilation and circulation using tritium and ^{3}He, *J. Geophys. Res.*, *103*, 15,817–15,831, 1998.

Jenkins, W. J., and J. C. Goldman, Seasonal oxygen cycling and primary production in the Sargasso Sea, *J. Mar. Res.*, *43*, 465–491, 1985.

Jenkins, W. J., and D. W. R. Wallace, Traced based inferences of new primary production in the sea, in *Primary Production and Biogeochemical Cycles*, edited by P. G. Falkowski and A. D. Woodhead, pp. 299–316, Plenum, New York, 1992.

Killworth, P. D., D. B. Chelton, and R. A. DeSzoeke, The speed of observed and theoretical long extratropical planetary waves, *J. Phys. Oceanogr.*, *27*, 1946–1966, 1997.

Knap, A., T. D. Jickells, A. Pszenny, and J. Galloway, Significance of atmospheric-derived fixed nitrogen on productivity in the Sargasso Sea, *Nature*, *320*, 158–160, 1986.

Ledwell, J. R., A. J. Watson, and C. S. Law, Evidence of slow mixing across the pycnocline from an open ocean tracer-release experiment, *Nature*, *364*, 701–703, 1993.

LeTraon, P. Y., and F. Ogor, ERS-1/2 orbit improvement using TOPEX/POSEIDON: The 2-cm challenge, *J. Geophys. Res.*, *103*, 8045–8057, 1998.

LeTraon, P. Y., P. Gaspar, F. Bouyssel, and H. Makhmara, Using TOPEX/Poseidon data to enhance ERS-1 data, *J. Atmos. Oceanic Technol.*, *12*, 161–170, 1995.

Levitus, S., and T. P. Boyer, World Ocean Atlas 1994, vol. 4, Temperature, *NOAA Atlas NESDIS 4*, U.S. Dep. of Commer., Washington, D. C., 1994.

Levitus, S., R. Burgett, and T. P. Boyer, World Ocean Atlas 1994, vol. 3, Salinity. *NOAA Atlas NESDIS 3*, U.S. Dep. of Commer., Washington, D. C., 1994.

Lippert, A., and M. G. Briscoe, Observations and EOF analysis of low-frequency variability in the western part of the Gulf Stream Recirculation, *J. Phys. Oceanogr.*, *20*, 646–656, 1990.

Lipschultz, F., and N. J. P. Owens, An assessment of nitrogen fixation as a source of nitrogen to the North Atlantic Ocean, *Biogeochemistry*, *35*, 261–274, 1996.

Lohrenz, S. E., G. A. Knauer, V. L. Asper, M. Tuel, A. F. Michaels, and A. H. Knap, Seasonal and interannual variability in primary production and particle flux in the northwestern Sargasso Sea: U.S. JGOFS Bermuda Atlantic Time-series Study, *Deep Sea Res.*, *Part A*, *39*, 1373–1391, 1992.

McGillicuddy, D. J., and A. R. Robinson, Eddy induced nutrient supply and new production in the Sargasso Sea, *Deep Sea Res.*, *Part I*, *44*, 1427–1450, 1997.

McGillicuddy, D. J., A. R. Robinson, and J. J. McCarthy, Coupled physical and biological modeling of the spring bloom in the North Atlantic, II, Three dimensional bloom and post-bloom processes, *Deep Sea Res.*, *Part I*, *42*, 1359–1398, 1995.

McGillicuddy, D. J., Jr., A. R. Robinson, D. A. Siegel, H. W. Jannasch, R. Johnson, T. D. Dickey, J. McNeil, A. F. Michaels and A. H. Knap, Influence of mesoscale eddies on new production in the Sargasso Sea, *Nature*, *394*, 263–266, 1998.

McGillicuddy, D. J., Jr., R. Johnson, D. A. Siegel, A. F. Michaels, N. R. Bates, and A. H. Knap, Mesoscale variations of biogeochemical properties in the Sargasso Sea, *J. Geophys. Res.*, this issue.

McWilliams, J. C., et al., The local dynamics of eddies in the western North Atlantic, in *Eddies in Marine Science*, edited by A. R. Robinson, pp. 92–113, Springer-Verlag, New York, 1983.

McWilliams, J. C., W. B. Owens, and B. L. Hua, An objective analysis of the POLYMODE Local Dynamics Experiment, I, General formulation and statistical model selection, *J. Phys. Oceanogr.*, *16*, 483–504, 1986.

Menzel, D. W., and J. H. Ryther, Annual variations in primary production of the Sargasso Sea off Bermuda, *Deep Sea Res.*, *7*, 282–288, 1961.

Michaels, A. F., and A. H. Knap, Overview of the U.S. JGOFS Bermuda Atlantic Time-series Study and the Hydrostation S program, *Deep Sea Res.*, *Part II*, *32*, 157–198, 1996.

Michaels, A. F., M. W. Silver, M. M. Gowing, and G. A. Knauer, Cryptic zooplankton swimmers in upper ocean sediment traps, *Deep Sea Res.*, *Part A*, *37*, 1285–1296, 1990.

Michaels, A. F., D. A. Siegel, R. Johnson, A. H. Knap, and J. N. Galloway, Episodic inputs of atmospheric nitrogen to the Sargasso Sea: Contributions to new production and phytoplankton blooms, *Global Biogeochem. Cycles*, *7*, 339–351, 1993.

Michaels, A. F., N. R. Bates, K. O. Buesseler, and A. H. Knap, Carbon imbalances in the Sargasso Sea, *Nature*, *372*, 537–540, 1994a.

Michaels, A. F., et al., Ocean time-series measurements off of Bermuda: The first two years of the U.S. JGOFS Bermuda Atlantic Time-series Study, *Deep Sea Res.*, *Part I*, *41*, 1013–1038, 1994b.

Michaels, A. F., D. Olson, J. L. Sarmiento, J. Ammerman, K. Fanning, R. Jahnke, A. H. Knap, R. Lipshultz, and J. Prospero, Inputs, losses and transformations of nitrogen and phosphorous in the pelagic North Atlantic Ocean, *Biogeochemistry*, *35*, 181–226, 1996.

Munk, W., Abyssal recipes, *Deep Sea Res.*, *13*, 707–730, 1966.

Musgrave, D. L., J. Chao, and W. L. Jenkins, Application of a model of upper ocean physics for studying seasonal cycles of oxygen, *J. Geophys. Res.*, *93*, 15,679–15,700, 1988.

Okubo, A., Oceanic diffusion diagrams, *Deep Sea Res.*, *18*, 789–802, 1971.

Oschlies, A., and V. Garçon, Eddy-induced enhancement of primary production in a model of the North Atlantic Ocean, *Nature*, *394*, 266–269, 1998.

Owens, W. B., J. R. Luyten, and H. L. Bryden, Moored velocity measurements on the edge of the Gulf Stream recirculation, *J. Mar. Res.*, *40*, suppl., 509–524, 1982.

Polito, P. S., and P. Cornillon, Long baroclinic Rossby waves detected by TOPEX/POSEIDON, *J. Geophys. Res.*, *102*, 3215–3235, 1997.

Prospero, J. M., K. Barrett, T. Church, F. Dentener, R. A. Duce, J. N. Galloway, H. Levy II, J. Moody, and P. Quinn, Atmospheric deposition of nutrients to the North Atlantic Basin, *Biogeochemistry*, *35*, 27–73, 1996.

Richardson, P. L., Eddy kinetic energy in the North Atlantic from surface drifters, *J. Geophys. Res.*, *88*, 4355–4367, 1983.

Richardson, P. L., A census of eddies observed in North Atlantic SOFAR float data, *Prog. Oceanogr.*, *31*, 1–50, 1993.

Richman, J. G., C. Wunsch, and N. G. Hogg, Space and time scales of mesoscale motions in the western North Atlantic, *Rev. Geophys.*, *15*, 385–420, 1977.

Riley, G. A., Phytoplankton of the north central Sargasso Sea, *Limnol. Oceanogr.*, *2*, 252–270, 1957.

Rintoul, S., and C. Wunsch, Mass, heat, oxygen and nutrient fluxes and budgets in the North Atlantic Ocean, *Deep Sea Res.*, *Part A*, *38*, 355–377, 1991.

Robinson, A. R., et al., Mesoscale and upper ocean variabilities during the 1989 JGOFS bloom study, *Deep Sea Res.*, *Part II*, *40*, 9–35, 1993.

Sarmiento, J. L., and C. Le Quéré, Oceanic carbon dioxide uptake in a model of century-scale global warming, *Science*, *274*, 1346–1350, 1996.

Sarmiento, J. L., G. Thiele, R. M. Key, and W. S. Moore, Oxygen and nitrate new production and remineralization in the North Atlantic Subtropical Gyre, *J. Geophys. Res.*, *95*, 18,303–18,315, 1990.

Sarmiento, J. L., R. Murnane, and C. Le Quéré, Air-sea CO_2 transfer and the carbon budget of the North Atlantic, *Philos. Trans. R. Soc. London*, *Ser. B*, *348*, 211–219, 1995.

Schroeder, E., H. Stommel, D. W. Menzel, and W. J. Sutcliffe, Climatic stability of eighteen degree water at Bermuda, *J. Geophys. Res.*, *64*, 363–366, 1959.

Siegel, D. A., and W. G. Deuser, Trajectories of sinking particles in the Sargasso Sea: Modeling of statistical funnels above deep-ocean sediment traps, *Deep Sea Res.*, *Part I*, *44*, 1519–1541, 1997.

Siegel, D. A., R. Iturriaga, R. R. Bidigare, H. Pak, R. C. Smith, T. D. Dickey, J. Marra, and K. S. Baker, Meridional variations of the springtime phytoplankton community in the Sargasso Sea, *J. Mar. Res.*, *48*, 379–412, 1990.

Siegel, D. A., A. F. Michaels, J. C. Sorensen, M. C. O'Brien, and M. A. Hammer, Seasonal variability of light availability and utilization in the Sargasso Sea, *J. Geophys. Res.*, *100*, 8695–8713, 1995.

Spitzer, W. S., and W. J. Jenkins, Rates of vertical mixing, gas exchange and new production: Estimates from seasonal gas cycles in the upper ocean near Bermuda, *J. Mar. Res.*, *47*, 169–196, 1989.

Stammer, D., Global characteristics of ocean variability estimated from regional TOPEX/POSEIDON altimeter measurements, *J. Phys. Oceanogr.*, *27*, 1743–1769, 1997.

Strass, V. H., Chlorophyll patchiness caused by mesoscale upwelling at fronts, *Deep Sea Res.*, *Part A*, *39*, 75–96, 1992.

Sverdrup, H. U., On the conditions for the vernal blooming of phytoplankton, *J. Cons. Cons. Perm. Int. Explor. Mer*, *18*, 287–295, 1953.

Talley, L. D., and M. E. Raymer, Eighteen degree water variability, *J. Mar. Res.*, *40*, suppl., 757–775, 1982.

The MODE Group, The mid-ocean dynamics experiment, *Deep Sea Res.*, *25*, 859–910, 1978.

Thiébaux, H. J., and M. A. Pedder, *Spatial Objective Analysis*, 299 pp., Academic, San Diego, Calif., 1987.

Washburn, L., D. A. Siegel, T. D. Dickey, and M. K. Hamilton, Isopycnal mixing and the distribution of particles across the North Pacific Subtropical Front, *Deep Sea Res.*, *Part A*, *36*, 1607–1620, 1989.

Washburn, L., D. C. Kadko, B. H. Jones, T. Hayward, P. M. Kosro, T. P. Stanton, S. Ramp, and T. Cowles, Water mass subduction and the transport of phytoplankton in a coastal upwelling system, *J. Geophys. Res.*, *96*, 14,927–14,945, 1991.

Williams, R. G., and M. J. Follows, The Ekman transfer of nutrients and maintenance of new production over the North Atlantic, *Deep Sea Res.*, *Part I*, *45*, 461–489, 1998.

Woods, J., Scale upwelling and primary production, in *Toward a Theory on Biological-Physical Interactions in the World Ocean*, edited by B. J. Rothchild, pp. 7–38, Kluwer Acad., Norwell, Mass., 1988.

Worthington, L. V., The 18° water in the Sargasso Sea, *Deep Sea Res.*, *5*, 297–305, 1959.

Worthington, L. V., On the North Atlantic circulation, *Johns Hopkins Oceanogr. Stud.*, *6*, 110 pp., 1976.

Wunsch, C., The vertical partition of oceanic kinetic energy and the spectrum of global variability, *J. Phys. Oceanogr.*, *27*, 1770–1794, 1997.

E. A. Fields and D. A. Siegel, Institute for Computational Earth System Science, University of California, Santa Barbara, CA 93106. (davey@icess.ucsb.edu)

D. J. McGillicuddy Jr., Department of Applied Ocean Physics and Engineering, Woods Hole Oceanographic Institution, Woods Hole, MA 02543.

(Received August 6, 1998; revised January 27, 1999;
accepted February 22, 1999.)